A novel variant in MFN2 linked to a lethal disorder of neonatal onset

Authors: Mashiat Zaman[1], Cole Chute[1], Julien L Marcadier[2], S Grewal[1], R Luke Wiseman[3], Amanda V Tyndall[4], Brenda McInnes[2], A Micheil Innes[5], Francois P Bernier[5], Timothy E. Shutt[6*]

[1]Department of Biochemistry & Molecular Biology, Cumming School of Medicine, Hotchkiss Brain Institute, Alberta Children's Hospital Research Institute, University of Calgary

[2]Department of Medical Genetics, Cumming School of Medicine, University of Calgary

[3]Department of Molecular and Cellular Biology, The Scripps Research Institute, La Jolla, CA

[4]Department of Medical Genetics, Cumming School of Medicine, Alberta Children's Hospital Research Institute, Hotchkiss Brain Institute, University of Calgary

[5]Departments of Medical Genetics and Pediatrics, Cumming School of Medicine, Alberta Children's Hospital Research Institute, University of Calgary

[6]Departments of Medical Genetics and Biochemistry & Molecular Biology, Cumming School of Medicine, Hotchkiss Brain Institute, Snyder Institute for Chronic Diseases, Alberta Children's Hospital Research Institute, University of Calgary

*Corresponding author (timothy.shutt@ucalgary.ca)

Abstract:

Pathogenic variants in the mitochondrial fusion protein Mitofusin2 typically cause axonal Charcot-Marie-Tooth disease type 2A (CMT2A), a progressively degenerative peripheral neuropathy. Here, we present three siblings with a lethal disorder of neonatal onset who carried a novel homozygous MFN2 variant R334K, which was predicted to be likely pathogenic. Given the severe clinical presentation, which is atypical of MFN2 variants, further functional investigations were warranted to confirm the pathogenicity of the R334K variant. Characterization of patient fibroblasts revealed severe disruptions in all MFN2-related functions assayed, including mitochondrial fragmentation, altered mito-ER contacts, decreased mtDNA copy number and size, increased lipid droplet abundance, and reduced mitochondrial respiration. We also observed reduced Complex I activity, which is noted in cells lacking MFN2, but is not typical of pathogenic MFN2 variants that cause CMT2A. Notably, re-expression of MFN2 R334K in MFN2 knockout cells was unable to rescue mitochondrial fragmentation and the Complex I deficiencies, confirming that the R334K variant is causative of these cellular phenotypes. Furthermore, disease modelling in *Drosophila melanogaster* demonstrated functional deficiencies of the R334K variant *in vivo*. Together, these findings confirm that the MFN2 R334K is a novel pathogenic variant causing severe fatal neonatal disease. Finally, we show that pharmacological activation of the integrated stress response rescues the defects caused by MFN2 R334K, offering a potential therapeutic avenue for MFN2 pathology.

37 **Introduction:**

38 Pathogenic variants in *MFN2* cause the hereditary motor sensory neuropathy Charcot-
39 Marie-Tooth disease 2a (CMT2a), which is characterized by progressive neuropathy with distal
40 numbness and weakness. CMT2a is generally considered as an early-onset disease, with
41 symptoms typically appearing around age 10. While CMT2a is most often autosomal dominant
42 (CMT2A2A), there are cases of homozygous or compound heterozygous recessive inheritance
43 (CMT2A2B) [25, 46]. *MFN2* encodes the integral outer mitochondrial membrane (OMM) protein
44 Mitofusin2 (MFN2), initially characterized for its role in mitochondrial fusion [12]. The protein
45 consists of distinct domains, with an N-terminal GTPase domain, followed by two coiled-coil
46 heptad repeat (HR) domains separated by a transmembrane domain.

47 The clinical presentation of CMT2a can vary widely, where some MFN2 variants are
48 associated with additional clinical features [29, 53, 54]. While there is evidence of specific
49 MFN2 variants leading to severe and early pathology, neonatal lethality is exceedingly rare [7,
50 13, 15, 21]. Though the reasons for this heterogeneity are unknown, it is notable that MFN2 has
51 several other functions, including mediating mito-ER contacts (MERCs) [10], facilitating mito-
52 lipid droplet contacts [9], participating in mitochondrial transport [40] and being a key regulator
53 of mitophagy [38]. These MFN2 functions also influence downstream processes such as mtDNA
54 regulation [55], cellular Ca^{2+} signalling [1] and mitochondrial bioenergetics [64]. The impact of
55 different MFN2 variants on the various functions of MFN2 is largely unknown [64]. Surprisingly,
56 for the few variants studied, fusion is not always impacted [2, 16, 30, 33, 63], suggesting that
57 other MFN2 functions are likely contributing to MFN2 pathogenesis.

58 There is currently no specific therapy for MFN2 pathologies. Although several promising
59 preclinical approaches are in development for CMT2A [49, 50, 62], they focus primarily on
60 promoting mitochondrial fusion, rather than other MFN2 functions. Building on the fact that
61 activation of the Integrated Stress Response (ISR) has recently garnered attention for
62 ameliorating mitochondrial dysfunction [1, 31, 40, 54], we recently showed that ISR activation
63 can restore mitochondrial morphology in patient fibroblasts harbouring the pathogenic D414V
64 MFN2 variant [5], as well as MERCs, mitochondrial motility, and mitochondrial respiration in

65 MFN2 KO cells [8] . ISR activation is mediated by phosphorylation of eIF2α via four kinases that
66 sense different types of cellular stress (*i.e.*, HRI, GCN2, PERK and PRK), ultimately turning on the
67 ATF4 transcription factor that engages multiple cellular stress responses. Thus, ISR activation is
68 a promising therapeutic approach to target mitochondrial dysfunction beyond just impaired
69 mitochondrial fusion.

70 In this work, we describe three siblings who presented with severe neonatal
71 encephalopathy with areflexia, limited spontaneous movements, respiratory failure, severe
72 hypotonia, arthrogryposis and neonatal demise. All three patients had novel homozygous
73 variants in MFN2, c.1001G>A, p.(Arg334Lys). We report detailed patient phenotypes and
74 provide a comprehensive characterization of multiple mitochondrial functions associated with
75 MFN2 in patient fibroblasts. Using cell and animal modelling, we provide evidence that the
76 R334K MFN2 variant significantly impacts mitochondrial function, not only explaining the
77 cellular phenotypes, but also being responsible for the neonatal lethal axonal disease reported
78 in these three siblings, thus expanding the clinical spectrum of CMT2A. Finally, we show that ISR
79 activation rescues mitochondrial fragmentation and reduced respiration in R334K patient
80 fibroblasts, offering a promising therapeutic avenue for MFN2-mediated pathology.

81 **Methods**

82 **Genomic analysis**

83 The proband was enrolled into a research study titled Rapid Access for Pediatric
84 Diagnoses Kidomics (RAPiD) at the Alberta Children's Hospital. Formal written consent was
85 provided by the family (mother, father, and proband) for both the RAPiD research exome (study
86 approved by the University of Calgary Conjoint Health Research Ethics Board) sequencing and
87 the clinical whole exome sequencing. DNA was extracted from whole blood samples, and trio
88 exome library preparation was conducted using the xGen Exome Research Panel v1.0 capture
89 kit (Integrated DNA Technologies, Inc., Coralville, IA, USA). Paired-end sequencing was
90 performed on a NextSeq 550 (Illumina, San Diego, CA, USA) in which data was automatically
91 uploaded into BaseSpace Sequencing Hub where alignment, variant calling, and variant
92 interpretation was completed.

93 **Sequence alignment**

94 Amino acid sequence alignments for MFN2 and FOXRED1 were performed on T-COFFEE
95 multiple sequence alignment tool [17]. Protein sequences were collected from the UniProt
96 database [58]. The UniProt Sequence ID's were as follows: Human MFN2: O95140-1; Human
97 MFN1: Q8IWA4; Mouse MFN2: Q80U63; Fish MFN2: A8WIN6; Fly MFN2: Q7YU24; Worm
98 MFN2: Q23424; FXRD1: Q96CU9; FXRD1 [2]: Q96CU9-2 ; FXRD1 [3]: Q96CU9-3; Mouse FXRD1:
99 Q3TQB2; Fish FXRD1: A0A0R4IHD6; Fly FXRD1: Q9VJ10; Worm FXRD1: A0A0V1BI76 .

100 **Cell culture**

101 Skin fibroblasts were cultured in Minimum Essential Media (Gibco™, 11095098),
102 supplemented with 10% Fetal Bovine Serum (FBS) and 10mM Sodium Pyruvate. The cells were
103 maintained at 37°C and 5% CO_2. U2OS cells were maintained in DMEM high-glucose media
104 (Gibco™; 11965118), also at 37°C and 5% CO_2. The following ISR inhibitors/activators were used
105 for the morphology and OCR studies: ISRIB (ISR inhibitor) (Cat# SML0843, Sigma), halofuginone
106 (Cat#50-576-3001, Sigma), #3610 or Parogrelil (139145-27-0, Axon Medchem). For drug

107 treatments the compounds were added at the following doses: ISRIB (200nM), compound
108 #3610 (10uM), Parogrelil (10uM) and Halofuginone (100nM),

109 **Respiration studies**

110 Cellular oxygen consumption rates were measured using the Seahorse XFe24
111 Extracellular Flux Analyzer (Agilent Technologies) as previously described [52]. In summary, cells
112 were seeded in the manufacturer provided microplate at 70,000 cells/well and incubated for 24
113 hours at 37°C and 5% CO_2. Subsequently, the growth media was replaced, and cells equilibrated
114 in assay media supplemented with d-Glucose (25 mM), sodium pyruvate (2 mM) and l-
115 Glutamine (4 mM). Oxygen consumption rates were calculated following administration of the
116 following compounds: Oligomycin (1 µg/mL) (Enzo Life Sciences, BML-CM111), Carbonyl
117 Cyanide 4-(trifluoromethoxy) Phenylhydrazone (FCCP, 1 µM) (Enzo life Sciences, BML-CM120)
118 and Antimycin A (1 µM) (Sigma Aldrich, A8674). The data from the Seahorse analyzer was
119 normalized to protein content data for each well measured by BCA assay (Thermo Fisher
120 Scientific, 23225). The Lucid Resipher assay was used for the ISR studies, as previously
121 described [8]. Briefly, 15,000 cells were seeded on a round bottom 96-well cell culture plate
122 (MaxBioChem, MBC.TC.F. 96)and allowed to settle for 18 hours. The ISR inhibitors/activators
123 were added at the following doses: ISRIB (200nM), compound #3610 (10uM), Parogrelil (10uM)
124 and Halofuginone (100nM):, and OCR was measured at 6 hours after treatment. Samples were
125 normalized for total protein content, lysed from the 96-well plate using RIPA buffer (Thermo
126 Scientific™, 89900) using a BCA assay, standardized with BSA (Fisher Scientific, PI23209).

127 **Immunofluorescence and Microscopy**

128 20,000 control/patient fibroblasts or U2OS cell lines were seeded on 12mm
129 (Fisherbrand, 12-545-81) coverslips inserted into wells of a 24-well plate (Sarstedt, 83.3922)
130 and incubated for 24 hours at 37°C and 5% CO_2. Cells were fixed with 4% paraformaldehyde
131 (ElectronMicroscopySciences, 15710) at 37°C for 20 minutes, permeabilized using 0.1% Triton®
132 X-100 (MP Biomedicals, 9002-93-1) and blocked with 10% FBS. The mitochondrial network was
133 stained with anti-TOMM20 (Sigma-Aldrich, HPA011562/Santa Cruz Biotechnology, F-10 sc-
134 17764) primary antibodies and visualized using goat anti-rabbit secondary conjugated with

135 Alexa Fluor 488 (ThermoFisher, A-11034) or goat anti-mouse conjugated Alexa Fluor
136 (ThermoFisher, A-31571). Mitochondrial nucleoids were visualized using anti-dsDNA antibody
137 (Developmental Studies Hybridoma Bank, AB_10805293) and goat anti-mouse secondary
138 conjugated with Alexa fluor 568 (ThermoFisher, A-11004), following permeabilization with 0.2%
139 Triton® X-100). Lipid droplets were studied using BODIPY™ 493/503 (Invitrogen, D3922). Live
140 cells were seeded onto 35mm live cell imaging dishes (Cellvis ,D35-20-1.5-N) and allowed to
141 settle for 24 hours. The BODIPY dye was subsequently added at 10uM concentration and
142 incubated for 30 minutes, after which the cells were washed three times with culture media
143 and then imaged. Confocal imaging was performed using Olympus spinning disc confocal.
144 Confocal imaging was performed using Olympus spinning disc confocal system (Olympus SD
145 OSR) (UAPON 100XOTIRF/1.49 oil objective). STED imaging was performed using Leica TauSTED
146 microscope. For the ISR studies, control and patient fibroblasts were seeded at 70,000 cells
147 onto 35mm live cell imaging dishes (D35-20-1.5-N, Cellvis) and allowed to settle for 24 hours.
148 Mitochondrial networks were stained with 100nM MitoTracker Green FM (M7514, Life
149 Technologies) for 30 minutes and subsequently washed with cell culture media three times. . Z-
150 stacks were captured using confocal imaging was performed using Olympus spinning disc
151 confocal system (Olympus SD OSR) (UPlanApo. 60X 1.50NA), including a cellVivo live cell
152 incubator system used to maintain cells at 37°C and 5% CO_2 , Mitochondrial morphology was
153 qualitatively scored based on appearance categorized into fused/intermediate/fragmented for
154 150 cells, spread across 3 biological replicates. Quantitative mitochondrial network analyses
155 were performed using MiNA on FIJI [59], also scored for 150 cells, spread across 3 biological
156 replicates. Lipid droplets number and size were quantified using the 'analyze particles' tool on
157 FIJI.

158 **Proximity Ligation Assay:**

159 The proximity ligation assay was performed as mentioned in [54]. All immunostaining
160 steps, including fixation, blocking and permeabilizing were the same as mentioned for
161 mitochondrial network studies. The Duolink® In Situ Proximity Ligation Assay (Millipore Sigma)
162 was used for this. The aforementioned anti-TOMM20 antibody was used to label the
163 mitochondria, while the ER was labelled using anti-Calnexin (mouse monoclonal, EMD

164 Millipore: MAB3126 (RRID:AB_2069152). Images were analyzed using confocal microscopy (as
165 described above) and PLA puncta were analyzed using the 'analyze particles' tool on FIJI.

166

167

168 **Western Blot Analysis**

169 Cells grown to the same confluency were collected and RIPA buffer (Thermo Scientific™,
170 89900) complimented with protease inhibitors (VWR, 97063-010) was used to lyse and collect
171 the protein extracts. For fly protein, 20 flies were homogenized and sonicated in RIPA buffer
172 (Thermo Scientific™, 89900). Following quantification of protein concentrations using a BCA
173 assay, standardized to BSA (Fisher Scientific, PI23209), 50 µg of total protein was loaded on an
174 SDS-PAGE gel. Subsequently, PVDF membranes (Bio-Rad, 1620177) were used for overnight
175 transfer of the blots. The blots were probed with the following antibodies: anti-MFN2 (Abnova,
176 H00009927-M03; 1:1000), anti-MFN1 (Cell Signaling Technology, D6E2S; 1:1000), anti-OPA1 (BD
177 Transduction Laboratories, 612607; 1:1000), anti-Actin (Sigma, A5316; 1:1000) anti-Actin for fly
178 membrane (DSHB, JLA20; 1:1000) and cocktail anti-OXPHOS Complex antibody (AbCam,
179 ab110411; 1:500). Complimentary horseradish peroxidase conjugated antibodies were used:
180 goat anti rabbit IgG, HRP linked Antibody (Cell Signaling Technology, 7074S) or goat anti-mouse
181 IgG-HRP (Santa Cruz Biotechnology, sc-2055). Blots were treated with the SuperSignal™ West
182 Femto Maximum Sensitivity Substrate (Thermo Scientific™, 34095), and luminescence
183 visualized with an Amersham Imager AI600.

184 **mtDNA Copy Number and mtDNA Deletions Analysis**

185 Total DNA was extracted and purified from control and patient fibroblasts seeded at
186 30,000 cells using the PureLink Genomic DNA Mini Kit (Thermo Fisher Scientific, K182001) using
187 the given protocol. Relative mtDNA copy number was analysed using QuantStudio 6 Flex Real-
188 Time PCR system (Thermo Fisher Scientific). The mtDNA and nuclear encoded housekeeping
189 gene 18S were amplified using the primers and reaction conditions described in [18]. Long
190 range PCR reactions were performed to examine mtDNA deletions. The following primers were

191 used for amplification of the mtDNA: 1482–1516 F:
192 ACCGCCCGTCACCCTCCTCAAGTATACTTCAAAGG; 1180–1146 R:
193 ACCGCCAGGTCCTTTGAGTTTTAAGCTGTGGCTCG. The Takara LA Taq Polymerase (Takara Bio,
194 RR002M) was used with 250ng total cellular DNA. PCR cycling conditions were 94°C for 1 min;
195 98°C for 10 s and 68°C for 11 min (step 2 and 3- 35 cycles); and a final extension cycle at 72°C
196 for 10 min, using an Eppendorf® 5331 MasterCycler Gradient Thermal Cycler. PCR products
197 were visualized by electrophoresis on a 0·6% agarose gel, run for approximately 18 h at 20 V.

198 **Complex-I Activity Assay**

199 The mitochondrial complex-I activity assay was performed using the Complex I Enzyme
200 Activity Dipstick Assay Kit (AbCam, ab109720) according to manufacturer instructions. Briefly,
201 50,000 cells were seeded into a six-well plate (Sarstedt, 83.3920) and collected the following
202 day. 10x Extraction buffer from the kit was added to the cell pellet and subsequently spun at
203 18,000 x g. Supernatants were collected and following homogenization, control and patient
204 samples were plated in the plate provided. Subsequently, the dipstick from the plate was added
205 and incubated for 45 minutes. Following washing procedures, the dipsticks were imaged with
206 Amersham Imager AI600.

207 **Re-expression of MFN2 R334K in U2OS cells:**

208 U2OS MFN2 knockout cells were a generous gift from Dr. Edward Fon (McGill University,
209 Canada) [38]. The MFN2 R334K variant was inserted into MFN2 KO cells as previously described
210 [63]. Briefly, a retroviral plasmid vector (Vector Builder, VB230626-1399nzw) with the MFN2
211 R334K open reading frame or WT MFN2, followed by an mNeonGreen (after IRES) was virally
212 inserted into MFN2 KO cells, and cells were sorted for mNeonGreen expression through
213 fluorescence activated cell sorting. Endogenous expression levels were quantified by western
214 blot analysis, as described in the western blot section of methods.

215 ***Drosophila* stocks, transgenic lines and experiments**

216 All *Drosophila* were maintained at 25°C and kept in standard food. Flies were allowed to
217 lay eggs on standard grape plates with yeast plated for two days before collection. *Drosophila*

218 stocks for ey3.5-Gal4 (BDSC#8221) was provided by Dr. William Brook (University of Calgary,
219 Canada), elav-Gal4, tub-Gal4 (BDSC#5138), act5c-Gal4 (BDSC#4414), daGal4, UAS-*mCherry*RNAi
220 and UAS-*marf* RNAi (31157) [44] was provided by Dr. Savraj Grewal (University of Calgary,
221 Canada) and tincΔ4Gal4 was provided by Dr. Rolf Bodmer (Sanford Burnham Prebys Medical
222 Discovery Institute, USA). A second UAS-*marf*RNAi (67158) was purchased from Bloomington
223 Stock Centre (Indiana University, USA). Flies re-expressing the human MFN2 WT and MFN2
224 R334K were generated through microinjection (GENOMEPROLAB, Canada). The pGW.UAS
225 hMFN2 plasmid used for microinjection was provided by Dr. Paul Marcogliese (University of
226 Manitoba, Canada), which was subsequently mutated by in-fusion cloning (Takara, 638945).
227 Flies were microinjected on chromosome II using the attp40 landing site, through the phiC31
228 integration approach. For the survival assay, flies were allowed to lay eggs on grape plates with
229 yeast paste for 48 hours and subsequently 50 eggs were collected and placed into standard
230 food. The number of eggs that became pupa were counted and normalized to total number of
231 eggs collected, for percentage survival. For negative geotaxis studies, 30 newly emerged adult
232 flies of the respective crosses were placed into a 1000cc cylinder. On a given day, the flies were
233 gently displaced to the bottom every 3 hours and the percentage of flies that made it past the
234 10 cm mark after 10 seconds was counted.

235 **Statistical Analyses**

236 All statistical analyses were performed using GraphPad Prism 9.

237 **Results:**

238 **Case description:**

239 Proband (P1)

240 The male proband was born by C-section for preterm labor, breech presentation and
241 fetal heart rate abnormalities at 35 weeks to a 21-25-year-old G3, P0 mother. The pregnancy
242 was remarkable only for a mild COVID infection in the first trimester, with three antenatal
243 ultrasounds reported as completely normal. Decreased fetal movements were noted in the last
244 4 to 8 weeks of the pregnancy. His birthweight was 2.08 kg (10th percentile), length 46.6 cm
245 (50th percentile) and his head circumference was 32.1 cm (50th percentile). APGARs were
246 1,3,3,6 at 1, 5,10 and 15 minutes respectively. He remained flat with no respiratory effort and
247 was intubated at 6 minutes of life. He remained ventilator dependent and eventually died in
248 the pediatric intensive care unit at 2-6 weeks of age. On examination, he was noted to have
249 hypotonia both peripherally and axially with decreased spontaneous movements. He had
250 bilateral elbow and knee flexion contracures, with limited hip abduction, and talipes
251 equinovalgus. He was noted to have a bulbous nasal tip, but a complete dysmorphology exam
252 was not feasible.

253 Investigations included normal newborn metabolic screening, normal rapid aneuploidy
254 detection, SNP chromosomal microarray, Prader Willi, DM-1 and SMA. While chromosomal
255 microarray analysis did not reveal any copy number variation to explain the proband's
256 phenotype, the SNP component of the analysis revealed three contiguous regions (greater than
257 10Mb) of absence of heterozygosity (AOH) within chromosomes 1, 3, and 4. Metabolic
258 investigations revealed normal urine and plasma amino acids and a normal plasma acylcarnitine
259 profile. Urine organic acids were non diagnostic and plasma 3-methylglutaconic acid and 3-
260 methylglutaric acid were also normal. EEG was indicative of moderate diffuse/multifocal
261 cerebral dysfunction with multifocal epileptiform discharges. Brain MRI shortly after birth
262 showed multiple foci of diffusion restriction due to cytotoxic edema involving the deep and
263 periventricular white matter in frontoparietal lobes with corresponding intrinsic T1
264 hyperintensity. There were no overt signs on imaging or MRS to suggest a metabolic cause. A

265 follow-up brain MRI just prior to death reported interval resolution of the multiple foci of
266 restricted diffusion in the bilateral centrum semiovale ovale/corona radiata, with a few small
267 scattered residual centrum semiovale T1 hyperintense foci without restricted diffusion. As
268 compared to the previous MRI, there was interval development of atrophy of the superior
269 vermis, seen as increased interfoliate distance. Mild atrophy was also seen involving the lateral
270 cerebellar hemispheres. The brain stem structures, especially the midbrain and pons, had
271 reduced volume for patient's age, with prominence of the prepontine cisterns, resulting in
272 prominence of the posterior fossa CSF spaces without mass effect. The remainder of the
273 midline structures appeared normal with no Chiari I deformity and a normal pituitary gland. The
274 corpus callosum was well developed and the remaining brain parenchyma was normal with an
275 age-appropriate myelination pattern. No new areas of restricted diffusion or abnormal signal
276 involving the cerebrum or cerebellum were observed and there was no abnormal susceptibility-
277 related signal loss to suggest blood degradation products. The brain stem structures, especially
278 the midbrain and pons had reduced volume for the patient’s age. Additional imaging of the
279 patient’s spine showed marked smooth hypoplasia and reduced caliber of the thoracic spinal
280 cord. In addition, the brainstem and thoracic spinal cord reported to be small.

281 A muscle biopsy was performed shortly before death revealing no definite abnormalities
282 but coarse NADH, SDH, and COX histochemistries were observed in addition to mild
283 mitochondrial aggregation in the subarcolemmal spaces with some smaller mitochondria but
284 normal cristae. There were grouped atrophic fibres and occasional hypertrophic fibres.

285 He was born to healthy Middle Eastern parents who were known to be distantly
286 consanguineous. There was no family history of similarly affected children.

287 Proband's sibling (P2)

288 The proband's male sibling presented with the same core phenotype of encephalopathy,
289 hypotonia, hyporeflexia, arthrogryposis. The sibling had an unremarkable prenatal history with
290 normal anatomy scan. A second scan at revealed breech presentation but otherwise normal
291 with normal fetal movements. A further scan was appropriate for gestational age and showed
292 breech presentation. He was born via C-section due to preterm labor with APGARS 1, 2, and 3

293 at 1, 5 and 10 minutes respectively, with no spontaneous respirations. He was intubated and
294 admitted to NICU. He required continuous mandatory ventilation. Life sustaining measures
295 were withdrawn between day 11-15 and the patient died the same day. An autopsy was
296 declined.

297 On examination at birth, the baby was noted to be hypotonic with contractures and
298 decreased range of motion of elbows, hips and knees with bilateral talipes equinovarus. His
299 birth weight was 2.365kg (<50th percentile), length 48 cm (<90th percentile) and head
300 circumference 31.4 cm (50th percentile). He had depressed/absent reflexes. Investigations
301 included a normal newborn metabolic screen, normal lactates, ammonia, and liver enzymes
302 with a mildly elevated CK. An EEG was consistent with encephalopathy. Brain MRI showed
303 cerebellar hypoplasia with query germiolytic cysts. An MRI of the spine was normal.

304 Proband's sibling (P3)

305 A third affected child presented with very similar features to other affected siblings. Prenatal
306 ultrasounds at 23-27 weeks revealed suspected club feet, and the fetus was in breech
307 presentation at 32-36 weeks, which raised concerns regarding a likely recurrence of what was
308 now clearly suspected to be a recessive disorder. Delivery was by emergent C-section with
309 APGARS of 1,2,4. The neonatal presentation was very similar to the siblings, with severe
310 encephalopathy, limited respiratory effort, no large joint spontaneous movements or
311 spontaneous eye opening, and arthrogryposis requiring admission to NICU for ventilation. No
312 seizures were identified, and the EEG was encephalopathic with prolonged interburst intervals.
313 MRI features were also consistent with those of the previous affected children with hypoplasia
314 of the parietal lobes, cerebellum, and upper cord. The goal of care was changed at 3-7 days of
315 life, and this girl passed shortly after extubation.

316 **Genetic workup**:

317 Upon initial research RAPID exome sequencing, trio analysis of P1 and parents, who
318 were distantly consanguineous, detected the homozygous c.1001G>A, p.(Arg334Lys) variant of
319 uncertain significance in the MFN2 gene. Pathogenic variants in MFN2 are associated with
320 autosomal dominant and autosomal recessive Charcot-Marie-Tooth disease, axonal, type 2A.

321 While patients with variants in MFN2 have a heterogeneous clinical presentation with an age of
322 onset ranging from 1-45 years, previously reported individuals with homozygous or compound
323 heterozygous variants presented before the age of 10 years [41, 57]. These affected individuals
324 presented with muscle weakness, distal sensory loss, and normal or mildly decreased nerve
325 conduction velocity, while the heterozygous parents were reported to be asymptomatic or had
326 signs of a mild peripheral neuropathy [41]. This variant has not been reported in gnomAD,
327 ClinVar, or the literature. This missense variant resides near the middle of exon 10 of 19 and
328 appears to abolish a potential cryptic donor splice site within this exon. The consequence of the
329 loss of this cryptic donor splice site is unknown. A subsequent clinical exome of P1 confirmed
330 the homozygous MFN2 c.1001G>A, p.(Arg334Lys) variant, and also found a novel homozygous
331 missense variant of unknown significance, c.1454T>A, p.(Ile485Asn), in FOXRED1, a gene
332 associated with complex I deficiency [4, 20, 22, 31].

333 Sanger sequencing was used to assess the genetic status of P2. Analysis found
334 homozygosity for MFN2 Arg334Lys, but only heterozygosity for FOXRED1 Ile485Asn. The family
335 also had an unaffected sister, for whom no genetic information was obtained.

336 Based on the genetic work-up from P1, we initially considered both MFN2 R334K and
337 FOXRED1 I485N variants. Given that the candidate variants in MFN2 and FOXRED1 have not
338 been described or characterized previously, we examined the conservation of the
339 corresponding amino acid changes in the protein. We found that the MFN2 R334 residue is
340 conserved in multiple species, including fruit flies and worms, as well as in the paralogous
341 protein MFN1, arguing that it plays an important role in protein function (Figure 1a).
342 Meanwhile, though the FOXRED1 I485 residue is conserved in vertebrates, it is not conserved in
343 earlier diverging metazoans such as flies or worms (Figure 1b). Upon subsequent sequencing of
344 P2, who was homozygous for MFN2 R334K, but only heterozygous for and FOXRED1 I485N, it
345 became evident that MFN2 R334K was most likely the causative variant for the remarkably
346 consistent phenotype in the two brothers. Topologically, the MFN2 R334K variant is near the
347 GTPase domain (Figure 1c), which is crucial for mitochondrial fusion [32].

348 **Characterization of patient fibroblasts harboring MFN2 R334K:**

349 As the candidate pathogenic variant in MFN2 is novel and has not been characterized
350 previously, fibroblasts from a skin biopsy of P1, who harboured homozygous MFN2 R334K and
351 FOXRED1 I485N variants, were obtained for functional analysis. We examined a variety of
352 cellular and mitochondrial phenotypes to see which, if any, might be consistent with MFN2
353 and/or FOXRED1 dysfunction. Unfortunately, fibroblast cells were not available for P2.

354 **Patient fibroblasts show evidence of mitochondrial dysfunction:**

355 Given the integral role of mitochondria in ATP production, we first assessed oxygen
356 consumption in patient fibroblasts, as this is a key indicator of changes to mitochondrial
357 function. Compared to control cells, we observed marked decreases in both basal (around half)
358 and maximal (around two-third) oxygen consumption (Figure 2a), as well as spare respiratory
359 capacity (Figure 2b). These findings are indicative of severely reduced mitochondrial respiration
360 in patient fibroblasts, consistent with an underlying mitochondrial dysfunction contributing to
361 the patient phenotype.

362 Next, we investigated the canonical function of MFN2 in mitochondrial fusion by
363 visualizing the mitochondrial network after immunofluorescent labeling for the mitochondrial
364 marker TOMM20 (Figure 2c). In comparison to the control fibroblasts, which showed elongated
365 and reticular mitochondrial network morphology, patient fibroblasts qualitatively displayed
366 more fragmented mitochondrial networks (Figure 2d). Quantitative analysis of the
367 mitochondrial networks confirmed patient fibroblasts had shorter mitochondria (Figure 2e).
368 Together, these findings are consistent with impaired mitochondrial fusion leading to more
369 fragmented mitochondria.

370 **Changes in mitochondrial nucleoids and mtDNA copy number depletion in patient fibroblasts:**

371 To provide further evidence of impaired mitochondrial fusion, we investigated the
372 distribution and abundance of mtDNA, which can be altered by impairments to mitochondrial
373 fusion, are linked to loss of MFN2 function, and have been observed for some MFN2 variants
374 [48, 56, 64]. Immunofluorescence imaging of mtDNA nucleoids (Figure 3a) revealed that the
375 patient fibroblasts exhibited approximately half as many nucleoids as control fibroblasts (Figure
376 3b), and that patient mtDNA nucleoids were smaller (Figure 3c). Consistent with the reduced

377 number of mtDNA nucleoids, we detected a 40% decrease in the mtDNA copy number in the
378 patient fibroblasts via qPCR (Figure 3d). Finally, we also investigated the presence of mtDNA
379 deletions, which are sometimes seen with MFN2 loss of function [64]. However, no mtDNA
380 deletions were detected (Figure 3e).

381 **Altered mito-ER contact sites and lipid droplet accumulation in patient fibroblasts:**

382 We investigated the size and abundance of mito-ER contact sites (MERCs) and lipid
383 droplets, as these phenotypes can be altered in fibroblasts from patient harboring pathogenic
384 MFN2 variants [30, 54]. As a proxy for MERCs, we utilized a proximity ligation assay (PLA) that
385 generates a fluorescent signal when mitochondria and ER are within ~40 nm (Figure 4a-b) [6].
386 Using confocal microscopy, we observed a decrease in the size and number of MERCs, which
387 was confirmed by quantitative analyses (Figure 4c-d). We examined lipid droplets using the
388 neutral lipid droplet dye BODIPY 493/503 (Figure 5a). Compared to control fibroblasts, we
389 noted a distinct upregulation in the number (Figure 5b) and size (Figure 5c) of lipid droplet
390 puncta in the R334K patient fibroblasts. These findings of decreased MERCs and increased lipid
391 droplets are consistent with previously reported alterations in fibroblasts from patients with
392 CMT2A harbouring MFN2 variants [9, 30].

393 **MFN2 and mitochondrial protein expression:**

394 As our findings were consistent with MFN2 dysfunction, we assessed if expression of
395 MFN2 and other mitochondrial proteins was impacted. While we did not observe changes in
396 MFN2 protein levels from total cell lysate (Figure 6a-b), we did observe a significant (~50%)
397 decrease in expression of the nuclear DNA encoded mitochondrial complex I subunit NDUFB8
398 (Figure 6a/c). Notably, there was no consistent significant change to the levels of the other
399 OXPHOS proteins investigated here, including mtDNA-encoded MTCO1. The cause for this
400 discrepancy in OxPhos protein expression is unknown, but likely does not reflect the mtDNA
401 depletion, which would be expected to cause a global decrease in OxPhos protein expression as
402 mtDNA encodes essential proteins for all the electron transport chain complexes except for
403 complex II.

404 **Complex I activity:**

405 Given the specific decrease in a Complex I protein, which is not typical of MFN2
406 dysfunction and likely not explained by mtDNA depletion, we wondered if the identified
407 FOXRED1 missense variant might also have functional consequences that could contribute to
408 the patient phenotype. As pathogenic defects in FOXRED1 are linked to dysfunction in complex
409 I assembly and stability, we also examined Complex I activity. Consistent with the reduced
410 protein expression, and possible complex I instability, we observed an ~50% reduction in
411 Complex I activity in patient fibroblasts (Figure 6d-e).

412 ***In vitro* re-expression of MFN2 R334K recapitulates Complex-I deficiencies**

413 To test if the reduced Complex I activity in patient fibroblasts can be explained by the
414 MFN2 R334K variant alone, we used a knockout re-expression system to test the pathogenicity
415 of the R334K MFN2 variant in a different genetic background. Using U2OS MFN2 KO cells, we
416 re-expressed either the WT MFN2 protein or the MFN2 R334K variant by viral transduction,
417 selecting cells expressing endogenous levels of MFN2 expression (Figure 7c-d). To confirm the
418 system recapitulates features of patient fibroblasts, we first looked at mitochondrial
419 morphology. As expected, MFN2 KO cells had severely fragmented mitochondrial networks,
420 which were rescued by re-expression of the WT protein in KO cells (Figure 7a-b). In line with the
421 mitochondrial fragmentation observed in patient fibroblasts, we found that MFN2 KO cells re-
422 expressing MFN2 R334K show partial rescue compared to MFN2 KO cells, but remained more
423 fragmented than control cells or KO cells re-expressing WT MFN2. Next, we examined the
424 expression of OxPhos proteins and Complex I function. MFN2 KO cells had severe reductions in
425 Complexes I, II, III, and IV subunits, which were fully rescued by re-expressing WT MFN2.
426 However, although Complex II, III and IV protein expression was rescued in MFN2 KO cells re-
427 expressing the R334K variant, Complex I protein expression was reduced by ~50% compared to
428 controls (Figure 7c-d). Looking at Complex I activity, MFN2 KO cells showed a marked reduction
429 that was fully rescued by WT MFN2. Although cells re-expressing MFN2 R334K showed a partial
430 rescue compared to the KO, there was still a significant 50% decrease compared to controls
431 (Figure 7e-f). Taken together, these findings confirm previous work showing MFN2 loss of
432 function can lead to reduced Complex I activity [34, 45], and demonstrate that the MFN2 R334K
433 variant alone can explain the 50% decrease in Complex I activity observed in patient fibroblasts.

434 ***In vivo* modelling of MFN2 R334K in *Drosophila melanogaster:***

435 To model the pathogenicity of the R334K MFN2 variant *in vivo*, we used a knockdown
436 re-expression paradigm in *Drosophila* (Figure 8a) that has been used to study the function of
437 other human MFN2 variants [19]. In this approach, depleting the MFN2 orthologue in flies,
438 *marf*, can be rescued by re-expressing WT human MFN2 (*hMFN2*). First, we examined the effect
439 of whole-body knockdown/re-expression using three different driver lines: Actin (*act5c*-Gal4),
440 Tubulin (*tub*-Gal4) or Daughterless (*da*-Gal4). Whole-body knockdown of *marf* was larval lethal
441 for all three promoters tested. While *act5c*-Gal4 and *tub*-Gal4 showed no survival, the weaker
442 *da*-Gal4 driver had ~10% survival (Figure 8b). Meanwhile, re-expression of WT *hMFN2* rescued
443 survival to ~60% (Figure 8b), confirming the ability of the WT human MFN2 to function in flies.
444 In contrast, re-expression of MFN2 R334K was insufficient to rescue the larval lethality (Figure
445 8b) in any of the whole-body driver lines.

446 Next, given the larval lethality of the whole-body *marf* knockdown and MFN2 R334K re-
447 expression, we used a tissue-specific drivers to examine the effects in neurons (*elav*-Gal4) and
448 cardiomyocytes (*tin*-Gal4), which are relevant to the neuromuscular patient pathology.
449 Knockdown of *marf* in cardiomyocytes showed no significant lethality (Figure 8c). Next, we
450 assayed for locomotor function using a negative geotaxis climbing assay. We observed a
451 marked decrease in climbing ability of flies with knockdown of *marf*, which is nearly completely
452 rescued by re-expressing WT MFN2, but not by re-expression of MFN2 R334K (Figure 8d). Using
453 the neuronal driver, we saw 70% survival with *marf* knockdown, which was completely rescued
454 with WT MFN2, while MFN2 R334K had 95% survival (Figure 8e). In terms of climbing ability
455 with the neuron driver line *marf* knockdown also led to a significant decrease, which was
456 completely rescued by WT MFN2 climbing. In contrast, MFN2 R334K provided only a slight
457 rescue (Figure 8f). Importantly, we confirmed similar levels of WT MFN2 and MFN2 R334K in
458 our fly lines (Figure 8g). Overall, these data show that the MFN2 R334K variant has reduced
459 functionality and is unable to rescue *marf* knockdown *in vivo* to the same level as WT MFN2.
460 Moreover, the deficits seen with neuronal and cardiomyocyte-specific knockdown, reflect the
461 severe pathology seen in the patient.

462 **Pharmacologic ISR activation rescues MFN2 R334K dysfunction in patient cells**

463 Given our previous work showing ISR activation rescues mitochondrial fragmentation
464 and oxygen consumption in MFN2-deficient cells [5, 8], we speculated that ISR activation would
465 ameliorate dysfunction in MFN2 R334K patient fibroblasts. To this end, a 6-hour treatment with
466 three distinct ISR activators (Halofuginone, 3610, and Parogrelil) completely rescued
467 mitochondrial morphology in R334K patient fibroblasts (Figure 9a-b/Supplemental Figure 1a-d).
468 Furthermore, all three ISR activators also partially rescued OCR deficits (Figure 9c). Importantly,
469 co-treatment with the ISR inhibitor ISRIB prevented the rescue of both morphology and OCR for
470 all three compounds, confirming that this rescue is dependent on ISR activation, rather than
471 any potential off-target effects of the drugs. Overall, these findings show that pharmacological
472 ISR activation is beneficial for MFN2 dysfunction, even for severe perturbations such as those
473 caused by MFN2 R334K.

474 **Discussion:**

475 We report three siblings who presented with severe neonatal encephalopathy,
476 hypotonia, areflexia and arthrogryposis and all three were homozygous for a novel missense
477 variant in MFN2 p.(Arg334Lys). We speculate that the location of the R334K MFN2 variant is
478 crucial for proper protein function, possibly by altering the nearby GTPase domain of the
479 protein. Though CMT2A can be an early-onset disease that can eventually restrict patient
480 movement as the disease progresses, the patients reported here exhibited lack of movement at
481 birth, indicative of a much more severe neonatal onset. Moreover, all three patients
482 succumbed in infancy (<6 weeks) and we would consider this presentation as being neonatal
483 lethal with ventilation. No improvement was observed over their clinical courses. Although
484 areflexia and hypotonia phenotypes are not typical of CMT2A, there are a few previous reports
485 of both phenotypes in patients harbouring MFN2 variants with severe early-onset presentation
486 [35, 43, 48, 51, 57, 65]. However, the patients we report here presented with symptoms
487 immediately upon birth, as opposed to the examples in the previous reports, where symptoms
488 presented from 6-12 months. With respect to the early onset of severe phenotypes linked to
489 MFN2 dysfunction, there is a recent report of a patient with severe CNS complications who

490 harboured a homozygous 50 amino acid deletion in MFN2 with antenatal presentation that
491 resulted in pregnancy termination at 31 weeks [13]. In this regard, the fact that loss of MFN2
492 function leads to embryonic lethality in mice [12] and larval lethality in fruit flies [19], is
493 consistent with a severe loss of MFN2 function due to the R334K variant.

494 In support of the notion that the R334K variant impairs MFN2 functions, we observed
495 changes across all the functions we explored, including mitochondrial network morphology,
496 oxidative phosphorylation, complex I activity, MERCs, mtDNA copy number and nucleoids, as
497 well as cellular lipid droplets. These findings suggest that the novel R334K variant causes severe
498 dysfunction of the MFN2 protein. To our knowledge, there are no previously characterized
499 MFN2 CMT2a variants with defects across all these functions [64]. However, to some degree
500 this finding likely reflects the fact that few MFN2 variants have been characterized extensively
501 for their impact on MFN2 functions, highlighting our limited understanding of how MNF2
502 variants impact MFN2 functions. In terms of MFN2 variants associated with more severe
503 cellular phenotypes, it is notable that MFN2 variants that correlate with reduced mtDNA copy
504 number and impaired oxidative phosphorylation are reported in patients that tend to present
505 with earlier-onset and severe clinical outcomes [33, 54, 60]. Collectively, this evidence is
506 consistent with severe MFN2 dysfunction contributing to the very early onset of clinical
507 symptoms in the patients we report here.

508 Considering the additional homozygous FOXRED1 variant in P1, it is also worth briefly
509 discussing the 50% Complex I deficiency in this patient's fibroblasts, which is not typical of
510 pathogenic MFN2 variants. Notably, complete loss of MFN2 function can lead to a specific
511 deficit in Complex I expression and function [34], which we also observe in U2OS KO cells.
512 Moreover, Complex I dysfunction was also reported with the MFN2 variant harbouring a 50
513 amino acid deletion resulting in pregnancy termination [13]. Thus, MFN2 dysfunction alone is
514 sufficient to cause Complex I deficiency. Although FOXRED1 is a molecular chaperone important
515 for the assembly of mitochondrial complex I [22, 42], several lines of evidence argue against a
516 role for the FOXRED1 I485N the patients' phenotype. First, the patient phenotypes do not
517 match. Homozygous or compound heterozygous recessive FOXRED1 variants cause
518 mitochondrial complex I deficiency, nuclear type 19 (MC1DN19), where only a handful of cases

519 have been described [4, 11, 20, 22, 24, 27, 66]. Clinical phenotypes of MC1DN19 mimic
520 common mitochondrial disorders such as Leigh syndrome and mitochondrial encephalopathy
521 [11, 27, 36], including lactic acidosis and growth restrictions. In contrast, there was no evidence
522 of lactic acidosis in these patients. Meanwhile, though MC1DN19 patients can have hypotonia
523 [20, 27], and can also be diagnosed with restricted movement accompanying Leigh syndrome
524 [22], there are no reports of areflexia in FOXRED1 patients, who typically survive well past
525 infancy [4]. Secondly, the genetics also argue against I485N FOXRED1 variant contributing to
526 pathology, as FOXRED1 is autosomal recessive, while P2 was heterozygous for the I485N
527 FOXRED1 variant. Thus, despite the fact that novel I485N FOXRED1 variant reported here is
528 located at the C-terminus of the protein, similar to other pathogenic FOXRED1 variants
529 described to date, and the fact that FOXRED1 patient fibroblasts also have reduced Complex I
530 activity [20] (with patient myoblasts reported with deficiencies in both Complex I and Complex
531 II [66]), this variant was ruled out as a contributing factor for the phenotype of P1 and P2, who
532 had identical presentations. Finally, our results in MFN2 KO cells re-expressing the R334K
533 variant show that this variant alone is sufficient to cause a 50% decrease in Complex I activity,
534 fully explaining the loss of Complex I activity in patient fibroblasts.

535 As there is no cure for CMT2A or other MFN2-mediated pathology, it is notable that
536 pharmacological ISR activation ameliorates the dysfunctions tied to mitochondrial
537 fragmentation and impaired oxygen consumption in MFN2 R334K patient cells. Notably, one of
538 the ISR activators we tested, Parogrelil, is an FDA-approved drug that has passed phase I clinical
539 trials [26, 28]. However, before clinical use for MFN2 pathology, further work is needed to
540 decipher mechanisms of ISR-dependent rescue, benefits beyond cultured cells, as well as
541 temporal and dosage effects. Nonetheless, ISR activation is a promising therapeutic
542 intervention for MFN2-mediated pathology.

543 Rapid whole exome sequencing (WES) has repeatedly shown that a quicker time to
544 diagnosis guides goals of clinical care, including less failed treatments, and ultimately lowers
545 the financial burden on the health care system [14, 23, 37]. While previous reports suggests
546 that between 30-50% of WES cases are solved or partly solved by a known disease-associated
547 gene, additional cases may reveal novel genes of uncertain significance (GUS). This study

548 demonstrates the utility of rapid WES accompanied by functional experiments to assess these
549 GUS and provide a diagnosis. Functional studies also have the potential to discover new
550 treatment options for novel genes. However, as this study demonstrates, this is dependent
551 upon the damaging effects of the variant on the normal function of the gene and/or protein.
552 Regardless, this study demonstrates the value of collaboration between clinical and research
553 colleagues.

554 While we acknowledge the limitations of studying a novel protein variant in a single
555 family, our functional studies in cells (both in patient fibroblasts and MFN2 KO cells re-
556 expressing the R334K variant), and in an animal model clearly demonstrate that functional
557 impairment of the R334K MFN2 variant is sufficient to explain the observed cellular and patient
558 phenotypes. The fact that that U2OS cells re-expressing the R334K variant recapitulates the key
559 cellular phenotypes of mitochondrial fragmentation and reduced oxygen consumption show
560 that this variant, rather than the FOXRED1 variant or some other undetected variant, is
561 responsible for the observed mitochondrial dysfunction in patient fibroblasts. Meanwhile,
562 modeling of the R334K variant in *Drosophila* provides *in vivo* evidence that the R334K variant
563 can explain the severe early onset patient phenotypes. Thus, combined with clear genetic
564 evidence, this functional work strongly argues for R334K as a novel pathogenic MFN2 variant
565 causing a severe early onset pathology. This work also highlights the fact that MFN2
566 dysfunction can cause much more severe pathology than CMT2A typically recognized to be
567 associated with MFN2 variants.

568

569 **Acknowledgements**

570 The authors would like to thank the study participants and their family. We would also
571 like to thank Matthew Lines for his input on the manuscript. We would like to thank Dr. Paul
572 Marcogliese (University of Manitoba, Canada) for his expertise and technical guidance with the
573 *Drosophila* work.

574

575 **Conflict of Interests**

576 The authors declare that they have no conflict of interest.

577

578 **Author contributions**

579 Designed and/or performed and analyzed mitochondrial or *Drosophila* experiments, MZ,
580 CC, SG, RLW and TES; Clinical evaluation of patients and write up, JLM, BM, AMI, FPB; Analyzed
581 exome data AVP; Drafted the manuscript or figures, MZ, AVP, BM, TES. All authors discussed
582 the results and commented on the manuscript.

583

584 **Funding**

585 This work was supported by funds provided by the Canadian Institutes of Health
586 Research (TES) and the Alberta Children's Hospital Research Institute (Owerko Center) (MZ). MZ
587 was supported by a Hotchkiss Brain Institute International Recruitment Scholarship. The
588 funders had no role in study design, data collection and interpretation, or the decision to
589 submit the work for publication.

590 **Figure Legends:**

591

592 Figure 1: The MFN2 and FOXRED1 single nucleotide variants are conserved across species. (a)
593 Multiple sequence alignment data shows conservation of MFN2 at Arginine-334 and (b)
594 FOXRED1 conservation of Isoleucine 485. Accession numbers used for comparison are: MFN2:
595 O95140-1; O95140-2; MFN1: Q8IWA4; Mouse MFN2: Q80U63; Fish MFN2: A8WIN6; Fly MFN2:
596 Q7YU24; Worm MFN2: Q23424; FXRD1: Q96CU9; FXRD1 [2]: Q96CU9-2; FXRD1 [3]: Q96CU9-3;
597 Mouse FXRD1: Q3TQB2; Fish FXRD1: A0A0R4IHD6; Fly FXRD1: Q9VJ10; Worm FXRD1:
598 A0A0V1BI76. (c) Topological representation of Mitofusin 2, highlighting the position of MFN2
599 R334K on the GTPase domain.

600

601 Figure 2: MFN2 R334K leads to severe mitochondrial dysfunction: (a) SeaHorse Oxygen
602 Consumption Rate (OCR) indicating control and patient fibroblasts, measured using XF23
603 extracellular flux analyzer (2 biological replicates with 12 technical replicates). The error bars on
604 the graph indicate the mean OCR +/ SD. (b) Quantification of spare respiratory capacity in
605 control fibroblasts and patient fibroblasts (2 biological replicates with 12 technical replicates);
606 the bars indicate mean +/- SD, statistics are from an unpaired t-test. (c) Representative STED
607 confocal microscopy images showing mitochondrial network morphology in control vs MFN2
608 R334K patient fibroblasts, stained using anti-TOMM20. (d)Graphical representation of
609 qualitative analysis of mitochondrial branch appearance (fused/intermediate/fragmented),
610 from analysis of 150 images including 3 biological replicates, the bars indicate mean for each
611 category +/ SD, statistics are from an unpaired t-test. (e) Violin plot showing quantitative
612 analyses of mean mitochondrial branch length in control and patient fibroblasts (from 150 cells
613 including 3 biological replicates), with violin plots indicating median and interquartile range
614 (IQR), from an unpaired t-test. Statistical values indicate the following: ns $P > 0.05$, * $P \leq 0.05$,
615 **** $P \leq 0.0001$.

616

617 Figure 3: Alterations to mitochondrial DNA in patient fibroblasts. (a) Representative confocal
618 images showing DAPI (nucleus) and mitochondrial nucleoids (anti-dsDNA) co-localized with the
619 mitochondrial network (anti-TOMM20) for control (top panels) and patient fibroblasts (bottom
620 panels). (b) Quantitative analyses of number of mitochondrial nucleoids per cell in control and
621 patient fibroblasts, the colors indicate biological replicates, the lines indicate mean number of
622 mito-nucleoids per cell +/ SD, statistics are from an unpaired t-test. (c) Quantitative analyses of
623 average size(s) of mitochondrial nucleoids in control and patient fibroblasts, the colors indicate
624 biological replicates, with the lines showing mean +/ SD, statistics are from an unpaired t-test.
625 (d) Quantitative analysis of mtDNA copy number in control and patient fibroblasts, relative to
626 18S rDNA, the colors indicate biological replicates, bars indicate mean +/ SD, statistics are from
627 an unpaired t-test. (e) Representative image of agarose gel to detect mtDNA deletions using
628 0.6% agarose gel following long-range PCR to target mtDNA amplification and ladder shown on
629 the left. Statistics shown on the graph represent: ns $P > 0.05$, * $P \leq 0.05$, ** $P \leq 0.01$, **** $P \leq$
630 0.0001.

631

632 Figure 4: Changes to mito-ER contact sites in patient fibroblasts. (a) Top panel shows
633 representative confocal images of mitochondria (anti-TOMM20) and ER (anti-calnexin) co-
634 localization, MERCs (PLA probes) and merged images for control fibroblasts. The bottom panel
635 shows zoomed representation of boxed region. (b) Top panel shows representative confocal
636 images of mitochondria (anti-TOMM20) and ER (anti-calnexin) co-localization, MERCs (PLA
637 probes) and merged images for patient fibroblasts. The bottom panel shows zoomed
638 representation of boxed region. (c) Quantitative analyses of number of PLA signals (MERCs) per
639 cell in control and patient fibroblasts, colors indicate biological replicates, the violin plots show
640 distribution of data, while the lines indicate mean +/ SD, statistics are from an unpaired t-test.
641 (d) Quantitative analyses of average size(s) of PLA puncta (size of MERCs) in control and patient
642 fibroblasts bars indicate the mean size of PLA puncta +/ SD, statistics are from an unpaired t-
643 test. Statistics used in the graphs represent the following*** $P \leq 0.001$, **** $P \leq 0.0001$.

644

645 Figure 5: Changes to cellular lipid droplet accumulation in control and patient fibroblasts. (a)
646 Representative confocal images from control (top) and patient (bottom) fibroblasts stained for
647 lipid droplets using the neutral lipid droplet stain BODIPY™ 493/503. Quantification of average
648 number (b) and (c) size of lipid droplets per cell in control and patient fibroblasts using
649 BODIPY™ 493/503. The violin plots indicate median and interquartile ranges, colours indicate
650 biological replicates and statistics are from an unpaired t-test. The statistics shown are
651 represented by: **** $P \leq 0.0001$.

652

653 Figure 6: MFN2 R334K impedes levels and activity of OXPHOS Complex-I. (a) Representative
654 Western Blot images from control and MFN2 R334K patient fibroblasts showing protein levels
655 of MFN2 and the OxPhos complexes, as well as loading control Beta-Actin and mitochondrial
656 loading control HSP-60. (b) Quantification of MFN2 levels in control fibroblasts and patient
657 fibroblasts relative to Beta-Actin, colours indicate biological replicates, the bars indicate mean
658 levels of MFN2 +/ SD, statistics show an unpaired t-test. (c) Quantification of mitochondrial
659 OxPhos complexes (I-V) levels from Western Blot analyses in control and patient fibroblasts
660 normalized to cellular beta-actin levels, colours indicate biological replicates, the lines indicate
661 mean for each category mean +/ SD, statistics are from individual unpaired t-tests versus the
662 control. (d) Representative images showing dipsticks used to characterize relative complex I
663 activity in control and patient fibroblasts, using the complex I dipstick assay. (e) Quantification
664 of relative complex-I activity performed using complex-I dipstick assay in control and patient
665 fibroblasts, colours indicate biological replicates, while bars indicate mean for each category +/
666 SD, Statistics shown indicate: ns $P > 0.05$, *** $P \leq 0.001$, **** $P \leq 0.0001$.

667

668 Figure 7- *In vitro* modelling of MFN2 R334K shows failure to rescue mitochondrial
669 fragmentation and complex-I deficiencies. (a) Representative confocal images showing
670 mitochondrial network morphology, labelled using anti-TOMM20 antibody for WT U2OS, U2OS
671 MFN2 KO and re-expression of WT MFN2 or MFN2 R334K in KO cells. (b) Quantitative analyses
672 of mitochondrial network morphology represented by mean mitochondrial branch length,

673 colours indicate biological replicates, violins plots show the median branch length and inter-
674 quartile range, statistics were performed using a one-way ANOVA. (c) Representative western
675 blot images showing re-expression levels of MFN2 (WT/R334K) and corresponding levels of
676 OXPHOS complex subunits, as well as loading control beta-actin. (d) Quantitative analyses in
677 WT U2OS/MFN2 KO/WT re-expression/MFN2 R334K re-expression in KO cells showing levels of
678 proteins (MFN2 re-expression levels and OXPHOS complexes); the colours indicate biological
679 replicates, bars show the mean protein levels +/- SD, statistics are from an unpaired t-test. (e-f)
680 Complex-I dysfunction in U2OS MFN2 R334K re-expression cells with (e) representative images
681 showing complex-I activity dipsticks and (f) Quantitative analyses of complex-I dipstick assay,
682 the colours indicate biological replicates, the lines show mean complex I activity +/- SD,
683 statistics are from one-way ANOVA. The statistics represent the following: ns $P > 0.05$, ** $P \leq$
684 0.01, **** $P \leq 0.0001$.

685

686 Figure 8: In vivo analyses of MFN2 R334K using *Drosophila melanogaster* show lethality and
687 locomotor dysfunctions. (a) Schematic representing Gal4-UAS approach for human disease
688 modelling in *Drosophila melanogaster*, with Gal4 under the control of whole body/tissue
689 specific promoters leading to expression of UAS-hMFN2 on chromosome II (phiC31 integrase
690 approach) and UAS-*marf* RNAi on chromosome III. UAS-*mCherry* RNAi was used as a control for
691 the Gal4-UAS system. (b) Whole-body survival assay in control, *marf* knockdown and re-
692 expression of hMFN2 WT and MFN2 R334K fly lines using Actin (*act5c*-Gal4*)*, Tubulin (*tub*-Gal4)
693 and Daughterless (*da*-Gal4) driver lines. n=80 flies, with four independent replicates. Bars show
694 mean survivability +/- SD, statistics are from unpaired t-tests. (c) Tissue-specific survival assay
695 for cardiomyocytes, using control, *marf* knockdown and re-expression of hMFN2 WT and MFN2
696 R334K fly lines using tinman (*tin*-Gal4) driver line. n=80, with four independent replicates; The
697 bars on the graph show mean survival +/- SD, statistics are from unpaired t-tests. (d) Negative
698 geotaxis assay to look for climbing ability of flies with changes to cardiomyocytes *(tin)*
699 knockdown and re-expression of human MFN2, lines show mean +/- SD, statistics are from
700 unpaired t-tests at each time point for WT-re=expression vs R334K re-expression. (e) Tissue-
701 specific survival assay for neurons, using control, *marf* knockdown and re-expression of hMFN2

702 WT and MFN2 R334K fly lines using elav (*elav*-Gal4) driver line. n=80, with four independent
703 replicates; The bars on the graph show mean survival +/- SD, statistics are from unpaired t-
704 tests. (f) Negative geotaxis assay to look for climbing ability of flies with changes to neurons
705 *(elav)* knockdown and re-expression of human MFN2, lines show mean +/- SD, statistics are
706 from unpaired t-tests at each time point for WT-re-expression vs R334K re-expression.
707 (f)Representative Western Blot images showing expression of human MFN2 protein expression
708 in in control, *marf* knockdown and re-expression of hMFN2 WT and MFN2 R334K fly lines under
709 the control of *elav*-Gal4. (b) Statistics represent the followingns $P > 0.05$, * $P \leq 0.05$, ** $P \leq 0.01$,
710 **** $P \leq 0.0001$.

711

712 Figure 9: ISR activation rescues mitochondrial fragmentation and boosts cellular oxygen
713 consumption in MFN2 R334K patient cells. (a) Representative confocal images showing
714 mitochondrial network morphology using MitoTracker green for control fibroblasts vs MFN2
715 R334K patient fibroblasts treated with ISR activators/inhibitors for 6 hours with vehicle, #3610
716 (10uM), Parogrelil (10uM) and Halofuginone (100nM), along with ISRIB (200nM). (b)
717 Quantitative analyses of mitochondrial network morphology for control/patient fibroblasts
718 treated with ISR activators, points on the graph indicate biological replicates, lines show mean
719 mitochondrial branch length +/- SD, statistics come from one-way ANOVA. (c) Quantitative
720 analyses of cellular oxygen consumption rate measured using Resipher OCR, for control
721 fibroblasts and patient fibroblasts treated for 6 hours with vehicle, #3610 (10uM), Parogrelil
722 (10uM) and Halofuginone (100nM), along with ISRIB (200nM). Colours indicate biological
723 replicates, violin plots show the median OCR and IQR, one-way ANOVA. Statistics on the graphs
724 represent the following: ns $P > 0.05$, * $P \leq 0.05$, **** $P \leq 0.0001$.

725

726 Supplemental Figure S1: ISR activation rescues mitochondrial fragmentation and boosts cellular
727 oxygen consumption. (A) Representative confocal images showing mitochondrial network
728 morphology using MitoTracker green for control fibroblasts treated with the following ISR
729 activators/inhibitors for 6 hours with vehicle, #3610 (10uM), Parogrelil (10uM) and

730 Halofuginone (100nM), along with ISRIB (200nM). (b) Quantitative analyses of mitochondrial
731 network morphology for control fibroblasts treated with ISR activators, points indicate
732 biological replicates, bars show mean +/- SD, statistics represent a one-way ANOVA. (c)
733 Representative confocal images showing mitochondrial network morphology using MitoTracker
734 green for MFN2 R334K patient fibroblasts treated with ISR activators/inhibitors for 6 hours with
735 vehicle, #3610 (10uM), Parogrelil (10uM) and Halofuginone (100nM), along with ISRIB (200nM).
736 (d) Quantitative analyses of mitochondrial network morphology for patient fibroblasts, colours
737 indicate biological replicates, symbols indicate means of biological replicates, lines show mean
738 +/- SD, one-way ANOVA. (e) Quantitative analyses of cellular oxygen consumption rate
739 measured using Resipher OCR, for control fibroblasts and patient fibroblasts treated for 6 hours
740 with vehicle, #3610 (10uM), Parogrelil (10uM) and Halofuginone (100nM), along with ISRIB
741 (200nM). Colours indicate biological replicates, violin plots show median and IQR, statistics
742 represent a one-way ANOVA. Statistical symbols represent ns $P > 0.05$, * $P \leq 0.05$, **** $P \leq$
743 0.0001.

744

745 **References:**

746 1. Ainbinder A, Boncompagni S, Protasi F, Dirksen RT (2015) Role of Mitofusin-2 in mitochondrial
747 localization and calcium uptake in skeletal muscle. Cell Calcium 57:14–24. doi:
748 10.1016/j.ceca.2014.11.002

749 2. Amiott EA, Lott P, Soto J, Kang PB, McCaffery JM, DiMauro S, Abel ED, Flanigan KM, Lawson VH,
750 Shaw JM (2008) Mitochondrial fusion and function in Charcot-Marie-Tooth type 2A patient
751 fibroblasts with mitofusin 2 mutations. Exp Neurol 211:115–127. doi:
752 10.1016/j.expneurol.2008.01.010

753 3. Anderson NS, Haynes CM (2020) Folding the Mitochondrial UPR into the Integrated Stress
754 Response. Trends Cell Biol 30:428–439. doi: 10.1016/j.tcb.2020.03.001

755 4. Apatean D, Rakic B, Brunel-Guitton C, Hendson G, Bai R, Sargent MA, Lavoie PM, Patel M, Stockler-
756 Ipsiroglu S (2019) Congenital lactic acidosis, cerebral cysts and pulmonary hypertension in an
757 infant with FOXRED1 related complex I deficiency. Mol Genet Metab Rep 18:32–38. doi:
758 10.1016/j.ymgmr.2018.12.006

759 5. Baron KR, Oviedo S, Krasny S, Zaman M, Aldakhlallah R, Mathur P, Pfeffer G, Bollong MJ, Shutt T,
760 Grotjahn DA, Wiseman RL (2024) Pharmacologic Activation of Integrated Stress Response Kinases
761 Inhibits Pathologic Mitochondrial Fragmentation. eLife 13. doi: 10.7554/eLife.100541.1

762 6. Benhammouda S, Vishwakarma A, Gatti P, Germain M (2021) Mitochondria Endoplasmic
763 Reticulum Contact Sites (MERCs): Proximity Ligation Assay as a Tool to Study Organelle Interaction.
764 Front Cell Dev Biol 9:789959. doi: 10.3389/fcell.2021.789959

765 7. Bombelli F, Stojkovic T, Dubourg O, Echaniz-Laguna A, Tardieu S, Larcher K, Amati-Bonneau P,
766 Latour P, Vignal O, Cazeneuve C, Brice A, Leguern E (2014) Charcot-Marie-Tooth Disease Type 2A:
767 From Typical to Rare Phenotypic and Genotypic Features. JAMA Neurology 71:1036–1042. doi:
768 10.1001/jamaneurol.2014.629

769 8. Bora P, Zaman M, Oviedo S, Kutseikin S, Madrazo N, Mathur P, Pannikkat M, Krasny S, Chu A,
770 Johnson KA, Grotjahn DA, Shutt TE, Wiseman RL (2025) Drug Repurposing Screen Identifies an HRI
771 Activating Compound that Promotes Adaptive Mitochondrial Remodeling in MFN2-deficient Cells.
772 2025.06.23.660251

773 9. Boutant M, Kulkarni SS, Joffraud M, Ratajczak J, Valera-Alberni M, Combe R, Zorzano A, Cantó C
774 (2017) Mfn2 is critical for brown adipose tissue thermogenic function. EMBO J 36:1543–1558. doi:
775 10.15252/embj.201694914

776 10. de Brito OM, Scorrano L (2008) Mitofusin 2 tethers endoplasmic reticulum to mitochondria. Nature
777 456:605–610. doi: 10.1038/nature07534

778 11. Calvo SE, Tucker EJ, Compton AG, Kirby DM, Crawford G, Burtt NP, Rivas M, Guiducci C, Bruno DL,
779 Goldberger OA, Redman MC, Wiltshire E, Wilson CJ, Altshuler D, Gabriel SB, Daly MJ, Thorburn DR,
780 Mootha VK (2010) High-throughput, pooled sequencing identifies mutations in NUBPL and
781 FOXRED1 in human complex I deficiency. Nat Genet 42:851–858. doi: 10.1038/ng.659

782 12. Chen H, Detmer SA, Ewald AJ, Griffin EE, Fraser SE, Chan DC (2003) Mitofusins Mfn1 and Mfn2
783 coordinately regulate mitochondrial fusion and are essential for embryonic development. J Cell
784 Biol 160:189–200. doi: 10.1083/jcb.200211046

785 13. Chevrollier A, Bonnard AA, Ruaud L, Gueguen N, Perrin L, Desquiret-Dumas V, Guimiot F, Becker P-
786 H, Levy J, Reynier P, Gaignard P (2024) Homozygous MFN2 variants causing severe antenatal
787 encephalopathy with clumped mitochondria. Brain 147:91–99. doi: 10.1093/brain/awad347

788 14. Chung CCY, Leung GKC, Mak CCY, Fung JLF, Lee M, Pei SLC, Yu MHC, Hui VCC, Chan JCK, Chau JFT,
789 Chan MCY, Tsang MHY, Wong WHS, Tung JYL, Lun KS, Ng YK, Fung CW, Wong MSC, Wong RMS, Lau
790 YL, Chan GCF, Lee SL, Yeung KS, Chung BHY (2020) Rapid whole-exome sequencing facilitates
791 precision medicine in paediatric rare disease patients and reduces healthcare costs. Lancet Reg
792 Health West Pac 1:100001. doi: 10.1016/j.lanwpc.2020.100001

793 15. Chung KW (2006) Early onset severe and late-onset mild Charcot-Marie-Tooth disease with
794 mitofusin 2 (MFN2) mutations. Brain 129:2103–2118. doi: 10.1093/brain/awl174

795 16. Detmer SA, Chan DC (2007) Complementation between mouse Mfn1 and Mfn2 protects
796 mitochondrial fusion defects caused by CMT2A disease mutations. J Cell Biol 176:405–414. doi:
797 10.1083/jcb.200611080

798 17. Di Tommaso P, Moretti S, Xenarios I, Orobitg M, Montanyola A, Chang J-M, Taly J-F, Notredame C
799 (2011) T-Coffee: a web server for the multiple sequence alignment of protein and RNA sequences
800 using structural information and homology extension. Nucleic Acids Res 39:W13-17. doi:
801 10.1093/nar/gkr245

802 18. Eaton JS, Lin ZP, Sartorelli AC, Bonawitz ND, Shadel GS (2007) Ataxia-telangiectasia mutated kinase
803 regulates ribonucleotide reductase and mitochondrial homeostasis. J Clin Invest 117:2723–2734.
804 doi: 10.1172/JCI31604

805 19. Eschenbacher WH, Song M, Chen Y, Bhandari P, Zhao P, Jowdy CC, Engelhard JT, Dorn GW (2012)
806 Two rare human mitofusin 2 mutations alter mitochondrial dynamics and induce retinal and
807 cardiac pathology in Drosophila. PLoS One 7:e44296. doi: 10.1371/journal.pone.0044296

808 20. Fassone E, Duncan AJ, Taanman J-W, Pagnamenta AT, Sadowski MI, Holand T, Qasim W, Rutland P,
809 Calvo SE, Mootha VK, Bitner-Glindzicz M, Rahman S (2010) FOXRED1, encoding an FAD-dependent
810 oxidoreductase complex-I-specific molecular chaperone, is mutated in infantile-onset
811 mitochondrial encephalopathy. Hum Mol Genet 19:4837–4847. doi: 10.1093/hmg/ddq414

812 21. Feely SME, Laura M, Siskind CE, Sottile S, Davis M, Gibbons VS, Reilly MM, Shy ME (2011) MFN2
813 mutations cause severe phenotypes in most patients with CMT2A. Neurology 76:1690–1696. doi:
814 10.1212/WNL.0b013e31821a441e

815 22. Formosa LE, Mimaki M, Frazier AE, McKenzie M, Stait TL, Thorburn DR, Stroud DA, Ryan MT (2015)
816 Characterization of mitochondrial FOXRED1 in the assembly of respiratory chain complex I. Hum
817 Mol Genet 24:2952–2965. doi: 10.1093/hmg/ddv058

818 23. Freed AS, Clowes Candadai SV, Sikes MC, Thies J, Byers HM, Dines JN, Ndugga-Kabuye MK, Smith
819 MB, Fogus K, Mefford HC, Lam C, Adam MP, Sun A, McGuire JK, DiGeronimo R, Dipple KM, Deutsch

820 GH, Billimoria ZC, Bennett JT (2020) The Impact of Rapid Exome Sequencing on Medical
821 Management of Critically Ill Children. J Pediatr 226:202-212.e1. doi: 10.1016/j.jpeds.2020.06.020

822 24. Haack TB, Madignier F, Herzer M, Lamantea E, Danhauser K, Invernizzi F, Koch J, Freitag M, Drost R,
823 Hillier I, Haberberger B, Mayr JA, Ahting U, Tiranti V, Rötig A, Iuso A, Horvath R, Tesarova M, Baric
824 I, Uziel G, Rolinski B, Sperl W, Meitinger T, Zeviani M, Freisinger P, Prokisch H (2012) Mutation
825 screening of 75 candidate genes in 152 complex I deficiency cases identifies pathogenic variants in
826 16 genes including NDUFB9. J Med Genet 49:83–89. doi: 10.1136/jmedgenet-2011-100577

827 25. Hikiami R, Yamashita H, Koita N, Jingami N, Sawamoto N, Furukawa K, Kawai H, Terashima T, Oka
828 N, Hashiguchi A, Takashima H, Urushitani M, Takahashi R (2018) Charcot-Marie-Tooth disease type
829 2A with an autosomal-recessive inheritance: the first report of an adult-onset disease. J Hum
830 Genet 63:89–92. doi: 10.1038/s10038-017-0353-3

831 26. Hori M, Iwama T, Asakura Y, Kawanishi M, Kamon J, Hoshino A, Takahashi S, Takahashi K, Nakaike
832 S, Tsuruzoe N (2009) NT-702 (parogrelil hydrochloride, NM-702), a novel and potent
833 phosphodiesterase 3 inhibitor, suppress the asthmatic response in guinea pigs, with both
834 bronchodilating and anti-inflammatory effects. Eur J Pharmacol 618:63–69. doi:
835 10.1016/j.ejphar.2009.07.005

836 27. Hu C, Xu Q, Shen J, Wang Y (2021) Clinical and Genetic Characteristics of Mitochondrial
837 Encephalopathy Due to FOXRED1 Mutations: Two Chinese Case Reports and a Review of the
838 Literature. Front Neurol 12:633397. doi: 10.3389/fneur.2021.633397

839 28. Ishiwata N, Noguchi K, Kawanishi M, Asakura Y, Hori M, Mitani A, Ito Y, Takahashi K, Nishiyama H,
840 Shudo N, Takahashi S, Takahashi K, Tsuruzoe N, Nakaike S (2007) NT-702 (parogrelil hydrochloride,
841 NM-702), a novel and potent phosphodiesterase inhibitor, improves reduced walking distance and
842 lowered hindlimb plantar surface temperature in a rat experimental intermittent claudication
843 model. Life Sci 81:970–978. doi: 10.1016/j.lfs.2007.07.025

844 29. Kimura Y, Nishikawa A, Hashiguchi A, Etoh M, Yoshimura A, Asai K, Miyashita N, Takashima H, Sumi
845 H, Naka T (2022) An MFN2-related Charcot-Marie-Tooth Disease Patient with Optic Nerve Atrophy,
846 Neurogenic Bladder Dysfunction, and Diaphragmatic Weakness. Intern Med 61:1743–1747. doi:
847 10.2169/internalmedicine.6487-20

848 30. Larrea D, Pera M, Gonnelli A, Quintana-Cabrera R, Akman HO, Guardia-Laguarta C, Velasco KR,
849 Area-Gomez E, Dal Bello F, De Stefani D, Horvath R, Shy ME, Schon EA, Giacomello M (2019) MFN2
850 mutations in Charcot-Marie-Tooth disease alter mitochondria-associated ER membrane function
851 but do not impair bioenergetics. Hum Mol Genet 28:1782–1800. doi: 10.1093/hmg/ddz008

852 31. Lemire BD (2015) Evolution of FOXRED1, an FAD-dependent oxidoreductase necessary for
853 NADH:ubiquinone oxidoreductase (Complex I) assembly. Biochim Biophys Acta 1847:451–457. doi:
854 10.1016/j.bbabio.2015.01.014

855 32. Li Y-J, Cao Y-L, Feng J-X, Qi Y, Meng S, Yang J-F, Zhong Y-T, Kang S, Chen X, Lan L, Luo L, Yu B, Chen
856 S, Chan DC, Hu J, Gao S (2019) Structural insights of human mitofusin-2 into mitochondrial fusion
857 and CMT2A onset. Nat Commun 10:4914. doi: 10.1038/s41467-019-12912-0

858 33. Loiseau D, Chevrollier A, Verny C, Guillet V, Gueguen N, Pou de Crescenzo M-A, Ferré M, Malinge
859 M-C, Guichet A, Nicolas G, Amati-Bonneau P, Malthièry Y, Bonneau D, Reynier P (2007)
860 Mitochondrial coupling defect in Charcot-Marie-Tooth type 2A disease. Ann Neurol 61:315–323.
861 doi: 10.1002/ana.21086

862 34. Luo N, Yue F, Jia Z, Chen J, Deng Q, Zhao Y, Kuang S (2021) Reduced electron transport chain
863 complex I protein abundance and function in Mfn2-deficient myogenic progenitors lead to
864 oxidative stress and mitochondria swelling. FASEB J 35:e21426. doi: 10.1096/fj.202002464R

865 35. Madrid R, Guariglia SR, Haworth A, Korosh W, Gavin M, Lyon GJ (2020) Early-onset cerebellar
866 ataxia in a patient with CMT2A2. Cold Spring Harb Mol Case Stud 6:a005108. doi:
867 10.1101/mcs.a005108

868 36. Marra F, Lunetti P, Curcio R, Lasorsa FM, Capobianco L, Porcelli V, Dolce V, Fiermonte G, Scarcia P
869 (2021) An Overview of Mitochondrial Protein Defects in Neuromuscular Diseases. Biomolecules
870 11:1633. doi: 10.3390/biom11111633

871 37. McDermott H, Sherlaw-Sturrock C, Baptista J, Hartles-Spencer L, Naik S (2022) Rapid exome
872 sequencing in critically ill children impacts acute and long-term management of patients and their
873 families: A retrospective regional evaluation. Eur J Med Genet 65:104571. doi:
874 10.1016/j.ejmg.2022.104571

875 38. McLelland G-L, Goiran T, Yi W, Dorval G, Chen CX, Lauinger ND, Krahn AI, Valimehr S, Rakovic A,
876 Rouiller I, Durcan TM, Trempe J-F, Fon EA (2018) Mfn2 ubiquitination by PINK1/parkin gates the
877 p97-dependent release of ER from mitochondria to drive mitophagy. eLife 7:e32866. doi:
878 10.7554/eLife.32866

879 39. Mick E, Titov DV, Skinner OS, Sharma R, Jourdain AA, Mootha VK Distinct mitochondrial defects
880 trigger the integrated stress response depending on the metabolic state of the cell. eLife 9:e49178.
881 doi: 10.7554/eLife.49178

882 40. Misko A, Jiang S, Wegorzewska I, Milbrandt J, Baloh RH (2010) Mitofusin 2 is necessary for
883 transport of axonal mitochondria and interacts with the Miro/Milton complex. J Neurosci 30:4232–
884 4240. doi: 10.1523/JNEUROSCI.6248-09.2010

885 41. Nicholson GA, Magdelaine C, Zhu D, Grew S, Ryan MM, Sturtz F, Vallat J-M, Ouvrier RA (2008)
886 Severe early-onset axonal neuropathy with homozygous and compound heterozygous MFN2
887 mutations. Neurology 70:1678–1681. doi: 10.1212/01.wnl.0000311275.89032.22

888 42. Pagliarini DJ, Calvo SE, Chang B, Sheth SA, Vafai SB, Ong S-E, Walford GA, Sugiana C, Boneh A, Chen
889 WK, Hill DE, Vidal M, Evans JG, Thorburn DR, Carr SA, Mootha VK (2008) A mitochondrial protein
890 compendium elucidates complex I disease biology. Cell 134:112–123. doi:
891 10.1016/j.cell.2008.06.016

892 43. Pellino G, Faggioli R, Galuppi A, Leon A, Fusco C, Tugnoli V, Suppiej A (2021) Mitofusin 2: The
893 missing link between mtDNA maintenance defects and neurotransmitter disorders. Mitochondrion
894 61:159–164. doi: 10.1016/j.mito.2021.09.011

895 44. Perkins LA, Holderbaum L, Tao R, Hu Y, Sopko R, McCall K, Yang-Zhou D, Flockhart I, Binari R, Shim
896 H-S, Miller A, Housden A, Foos M, Randkelv S, Kelley C, Namgyal P, Villalta C, Liu L-P, Jiang X, Huan-
897 Huan Q, Wang X, Fujiyama A, Toyoda A, Ayers K, Blum A, Czech B, Neumuller R, Yan D, Cavallaro A,
898 Hibbard K, Hall D, Cooley L, Hannon GJ, Lehmann R, Parks A, Mohr SE, Ueda R, Kondo S, Ni J-Q,
899 Perrimon N (2015) The Transgenic RNAi Project at Harvard Medical School: Resources and
900 Validation. Genetics 201:843–852. doi: 10.1534/genetics.115.180208

901 45. Pich S, Bach D, Briones P, Liesa M, Camps M, Testar X, Palacín M, Zorzano A (2005) The Charcot–
902 Marie–Tooth type 2A gene product, Mfn2, up-regulates fuel oxidation through expression of
903 OXPHOS system. Human Molecular Genetics 14:1405–1415. doi: 10.1093/hmg/ddi149

904 46. Polke JM, Laurá M, Pareyson D, Taroni F, Milani M, Bergamin G, Gibbons VS, Houlden H, Chamley
905 SC, Blake J, Devile C, Sandford R, Sweeney MG, Davis MB, Reilly MM (2011) Recessive axonal
906 Charcot-Marie-Tooth disease due to compound heterozygous mitofusin 2 mutations. Neurology
907 77:168–173. doi: 10.1212/WNL.0b013e3182242d4d

908 47. Quirós PM, Mottis A, Auwerx J (2016) Mitonuclear communication in homeostasis and stress. Nat
909 Rev Mol Cell Biol 17:213–226. doi: 10.1038/nrm.2016.23

910 48. Renaldo F, Amati-Bonneau P, Slama A, Romana C, Forin V, Doummar D, Barnerias C, Bursztyn J,
911 Mayer M, Khouri N, Billette de Villemeur T, Burglen L, Reynier P, Bernabe Gelot A, Rodriguez D
912 (2012) MFN2, a new gene responsible for mitochondrial DNA depletion. Brain 135:e223, 1–4;
913 author reply e224, 1–3. doi: 10.1093/brain/aws111

914 49. Rizzo F, Bono S, Ruepp MD, Salani S, Ottoboni L, Abati E, Melzi V, Cordiglieri C, Pagliarani S, De
915 Gioia R, Anastasia A, Taiana M, Garbellini M, Lodato S, Kunderfranco P, Cazzato D, Cartelli D, Lonati
916 C, Bresolin N, Comi G, Nizzardo M, Corti S (2023) Combined RNA interference and gene
917 replacement therapy targeting MFN2 as proof of principle for the treatment of Charcot-Marie-
918 Tooth type 2A. Cell Mol Life Sci 80:373. doi: 10.1007/s00018-023-05018-w

919 50. Rocha AG, Franco A, Krezel AM, Rumsey JM, Alberti JM, Knight WC, Biris N, Zacharioudakis E,
920 Janetka JW, Baloh RH, Kitsis RN, Mochly-Rosen D, Townsend RR, Gavathiotis E, Dorn GW (2018)
921 MFN2 agonists reverse mitochondrial defects in preclinical models of Charcot-Marie-Tooth disease
922 type 2A. Science 360:336–341. doi: 10.1126/science.aao1785

923 51. Rouzier C, Bannwarth S, Chaussenot A, Chevrollier A, Verschueren A, Bonello-Palot N, Fragaki K,
924 Cano A, Pouget J, Pellissier J-F, Procaccio V, Chabrol B, Paquis-Flucklinger V (2012) The MFN2 gene
925 is responsible for mitochondrial DNA instability and optic atrophy “plus” phenotype. Brain 135:23–
926 34. doi: 10.1093/brain/awr323

927 52. Sabouny R, Wong R, Lee-Glover L, Greenway SC, Sinasac DS, Care4Rare Canada, Khan A, Shutt TE
928 (2019) Characterization of the C584R variant in the mtDNA depletion syndrome gene FBXL4,
929 reveals a novel role for FBXL4 as a regulator of mitochondrial fusion. Biochim Biophys Acta Mol
930 Basis Dis 1865:165536. doi: 10.1016/j.bbadis.2019.165536

931 53. Sawyer SL, Cheuk-Him Ng A, Innes AM, Wagner JD, Dyment DA, Tetreault M, Care4Rare Canada
932 Consortium, Majewski J, Boycott KM, Screaton RA, Nicholson G (2015) Homozygous mutations in
933 MFN2 cause multiple symmetric lipomatosis associated with neuropathy. Hum Mol Genet
934 24:5109–5114. doi: 10.1093/hmg/ddv229

935 54. Sharma G, Zaman M, Sabouny R, Joel M, Martens K, Martino D, De Koning APJ, Pfeffer G, Shutt TE
936 (2022) Characterization of a novel variant in the HR1 domain of MFN2 in a patient with ataxia,
937 optic atrophy and sensorineural hearing loss. F1000Res 10:606. doi:
938 10.12688/f1000research.53230.2

939 55. Sidarala V, Zhu J, Levi-D'Ancona E, Pearson GL, Reck EC, Walker EM, Kaufman BA, Soleimanpour SA
940 (2022) Mitofusin 1 and 2 regulation of mitochondrial DNA content is a critical determinant of
941 glucose homeostasis. Nat Commun 13:2340. doi: 10.1038/s41467-022-29945-7

942 56. Silva Ramos E, Motori E, Brüser C, Kühl I, Yeroslaviz A, Ruzzenente B, Kauppila JHK, Busch JD,
943 Hultenby K, Habermann BH, Jakobs S, Larsson N-G, Mourier A (2019) Mitochondrial fusion is
944 required for regulation of mitochondrial DNA replication. PLoS Genet 15:e1008085. doi:
945 10.1371/journal.pgen.1008085

946 57. Tan CA, Rabideau M, Blevins A, Westbrook MJ, Ekstein T, Nykamp K, Deucher A, Harper A, Demmer
947 L (2016) Autosomal recessive MFN2-related Charcot-Marie-Tooth disease with diaphragmatic
948 weakness: Case report and literature review. Am J Med Genet A 170:1580–1584. doi:
949 10.1002/ajmg.a.37611

950 58. UniProt Consortium (2023) UniProt: the Universal Protein Knowledgebase in 2023. Nucleic Acids
951 Res 51:D523–D531. doi: 10.1093/nar/gkac1052

952 59. Valente AJ, Maddalena LA, Robb EL, Moradi F, Stuart JA (2017) A simple ImageJ macro tool for
953 analyzing mitochondrial network morphology in mammalian cell culture. Acta Histochem 119:315–
954 326. doi: 10.1016/j.acthis.2017.03.001

955 60. Vielhaber S, Debska-Vielhaber G, Peeva V, Schoeler S, Kudin AP, Minin I, Schreiber S, Dengler R,
956 Kollewe K, Zuschratter W, Kornblum C, Zsurka G, Kunz WS (2013) Mitofusin 2 mutations affect
957 mitochondrial function by mitochondrial DNA depletion. Acta Neuropathol 125:245–256. doi:
958 10.1007/s00401-012-1036-y

959 61. Winter JM, Yadav T, Rutter J (2022) Stressed to death: Mitochondrial stress responses connect
960 respiration and apoptosis in cancer. Mol Cell 82:3321–3332. doi: 10.1016/j.molcel.2022.07.012

961 62. Zacharioudakis E, Agianian B, Kumar MV V, Biris N, Garner TP, Rabinovich-Nikitin I, Ouchida AT,
962 Margulets V, Nordstrøm LU, Riley JS, Dolgalev I, Chen Y, Wittig AJH, Pekson R, Mathew C, Wei P,
963 Tsirigos A, Tait SWG, Kirshenbaum LA, Kitsis RN, Gavathiotis E (2022) Modulating mitofusins to
964 control mitochondrial function and signaling. Nat Commun 13:3775. doi: 10.1038/s41467-022-
965 31324-1

966 63. Zaman M, Sharma G, Almutawa W, Soule TG, Sabouny R, Joel M, Mohan A, Chute C, Joseph JT,
967 Pfeffer G, Shutt TE (2025) The MFN2 Q367H variant reveals a novel pathomechanism connected to
968 mtDNA-mediated inflammation. Life Sci Alliance 8:e202402921. doi: 10.26508/lsa.202402921

969 64. Zaman M, Shutt TE (2022) The Role of Impaired Mitochondrial Dynamics in MFN2-Mediated
970 Pathology. Front Cell Dev Biol 10:858286. doi: 10.3389/fcell.2022.858286

971 65. Züchner S, De Jonghe P, Jordanova A, Claeys KG, Guergueltcheva V, Cherninkova S, Hamilton SR,
972 Van Stavern G, Krajewski KM, Stajich J, Tournev I, Verhoeven K, Langerhorst CT, de Visser M, Baas

973 F, Bird T, Timmerman V, Shy M, Vance JM (2006) Axonal neuropathy with optic atrophy is caused
974 by mutations in mitofusin 2. Ann Neurol 59:276–281. doi: 10.1002/ana.20797

975 66. Zurita Rendón O, Antonicka H, Horvath R, Shoubridge EA (2016) A Mutation in the Flavin Adenine
976 Dinucleotide-Dependent Oxidoreductase FOXRED1 Results in Cell-Type-Specific Assembly Defects
977 in Oxidative Phosphorylation Complexes I and II. Mol Cell Biol 36:2132–2140. doi:
978 10.1128/MCB.00066-16

(a)

Arginine 334

317 355

```
MFN2_HUMAN        AQGMPEGGGALAEGFQVRMFEFQNFERRFEECISQSAVK
MFN1_HUMAN        AQGMPESGVALAEGFHARLQEFQNFEQIFEECISQSAVK
MFN2_MOUSE        AQGMPEGGGALAEGFQVRMFEFQNFERQFEECISQSAVK
MFN2_FISH         AQGMPEAGGALAEGFQARMFEFQNFERRFEECISQSAVK
MFN_FRUITFLY_Tr   AKGNPPHMGAIAEGFQIRYFEFQDFERKFEECISQSAVK
MFN_WORM_Transm   ARGLVQK-AYQAEGHGTRALEFQNFERHFEHCISRSAIH

cons                :        ***.  *  ***:**: **.***:**::
```

(b)

Isoleucine 485

475 486

```
FXRD1_HUMAN       YLGEKIQENNI--I
FXRD1_MOUSE       YLGEKLQEYNI--L
FXRD1_FISH        IKKKPILERNI--V
FXRD1_FRUITFLY    IVDQPMFELNNVLS
FXRD1_WORM        LRGKTVKPECF---

cons                  : :
```

(c)

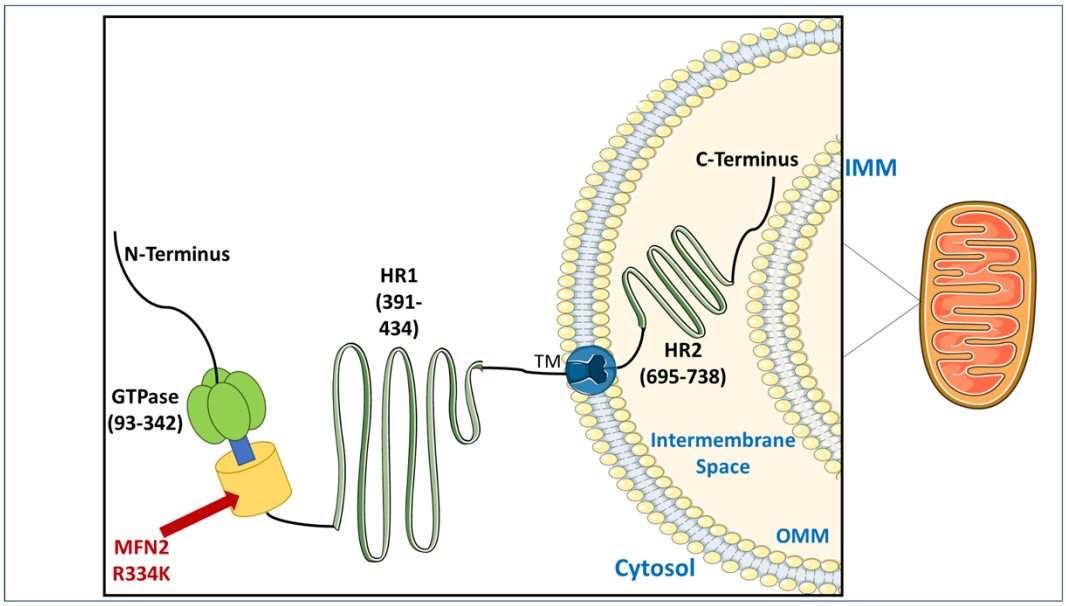

Figure 1

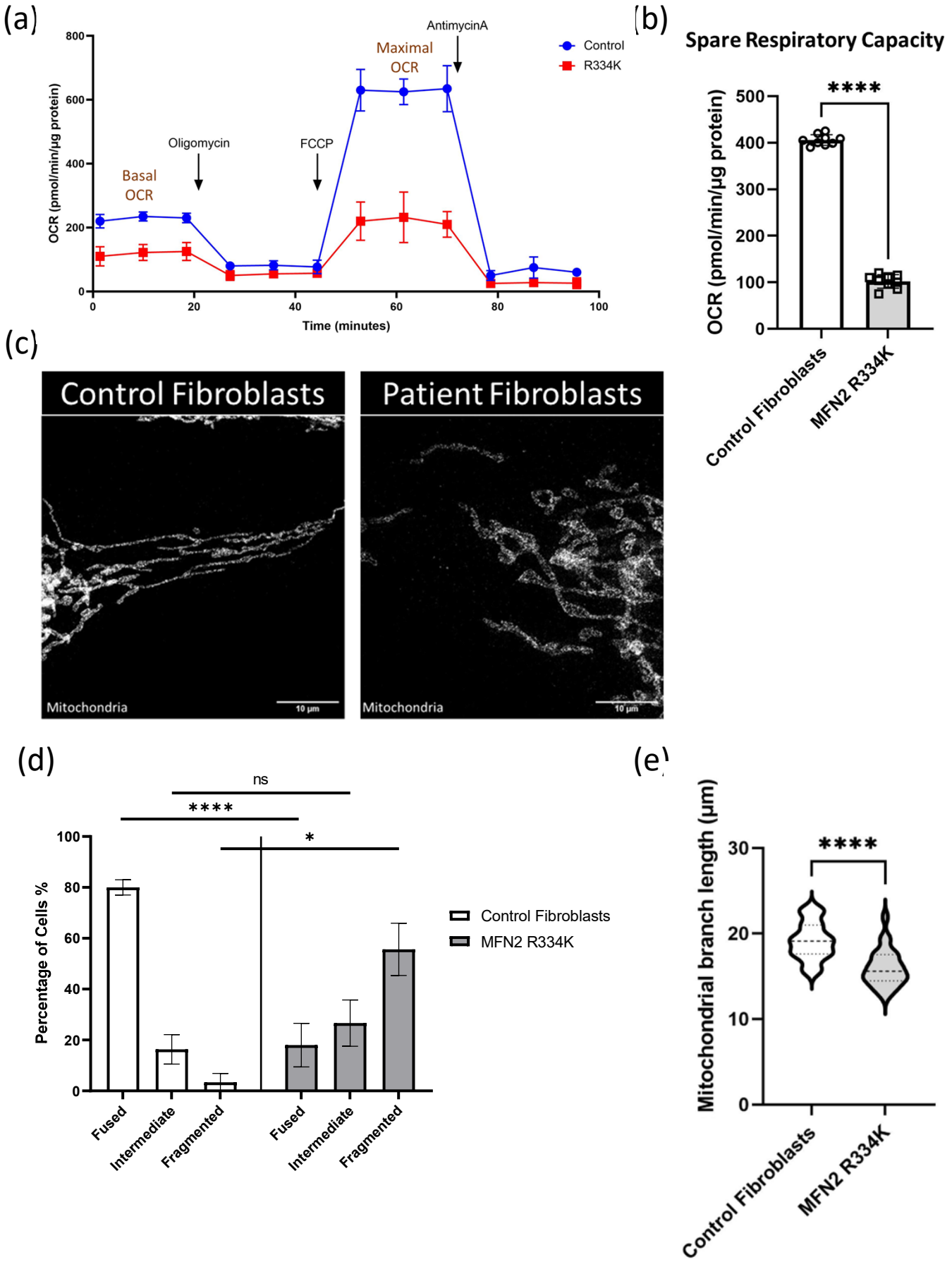
(a)
OCR (pmol/min/µg protein)
Time (minutes)
Basal OCR
Oligomycin
FCCP
Maximal OCR
AntimycinA
Control
R334K
(b)
Spare Respiratory Capacity
OCR (pmol/min/µg protein)
****
Control Fibroblasts
MFN2 R334K
(c)
Control Fibroblasts
Patient Fibroblasts
Mitochondria
10 µm
(d)
Percentage of Cells %
ns
****
*
Fused
Intermediate
Fragmented
Control Fibroblasts
MFN2 R334K
(e)
Mitochondrial branch length (µm)
****
Control Fibroblasts
MFN2 R334K

Figure 2

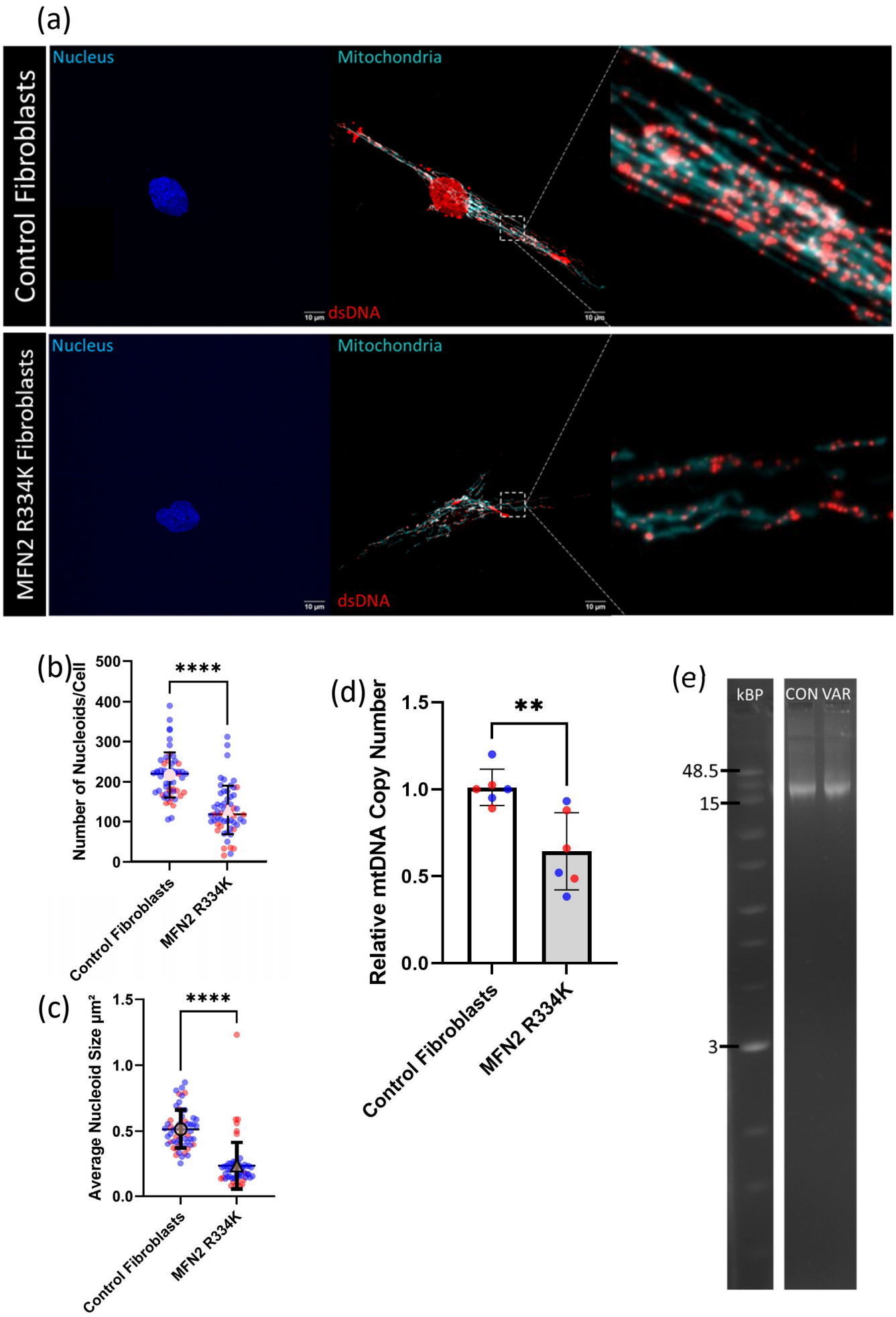
(a)
Control Fibroblasts
Nucleus
Mitochondria
dsDNA
MFN2 R334K Fibroblasts
Nucleus
Mitochondria
dsDNA
(b)
Number of Nucleoids/Cell
****
Control Fibroblasts
MFN2 R334K
(c)
Average Nucleoid Size µm²
****
Control Fibroblasts
MFN2 R334K
(d)
Relative mtDNA Copy Number
**
Control Fibroblasts
MFN2 R334K
(e)
kBP
CON VAR
48.5
15
3

Figure 3

(a)

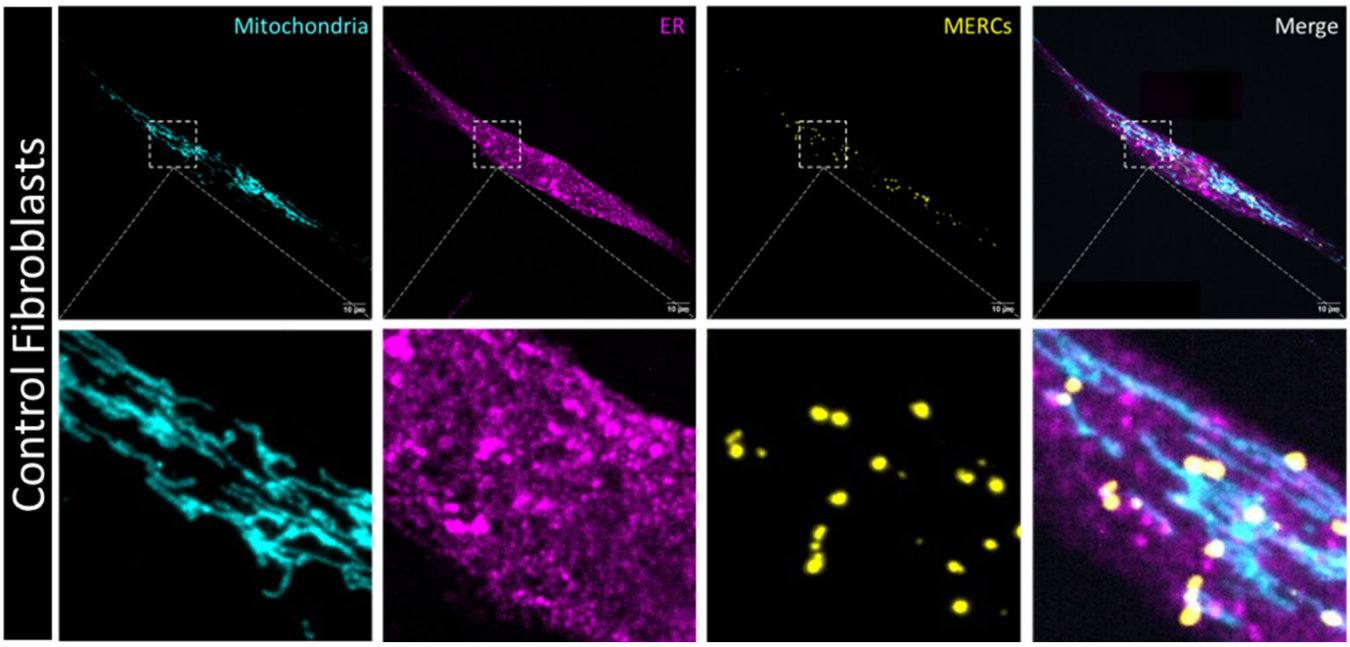

(b)

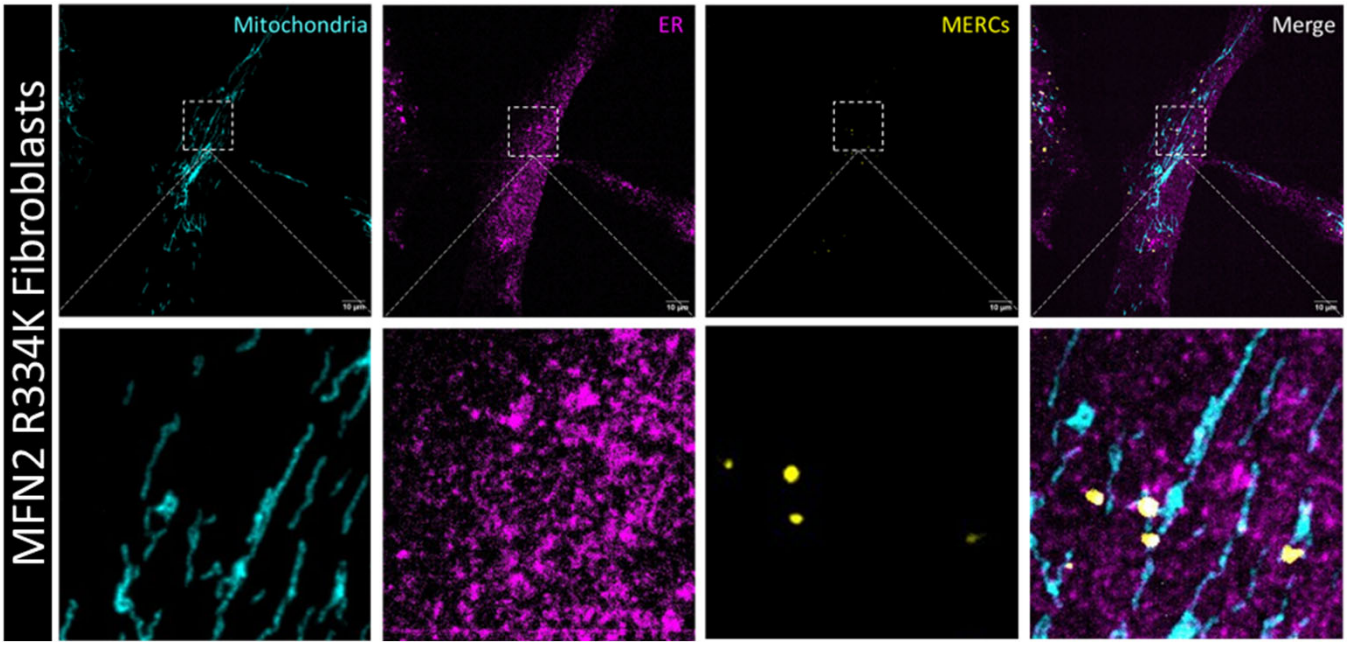

(c)

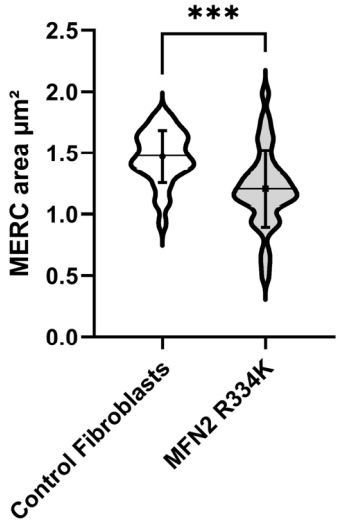

(d)

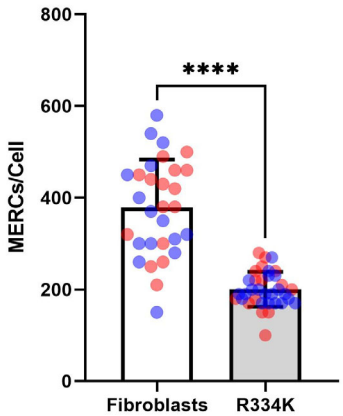

Figure 4

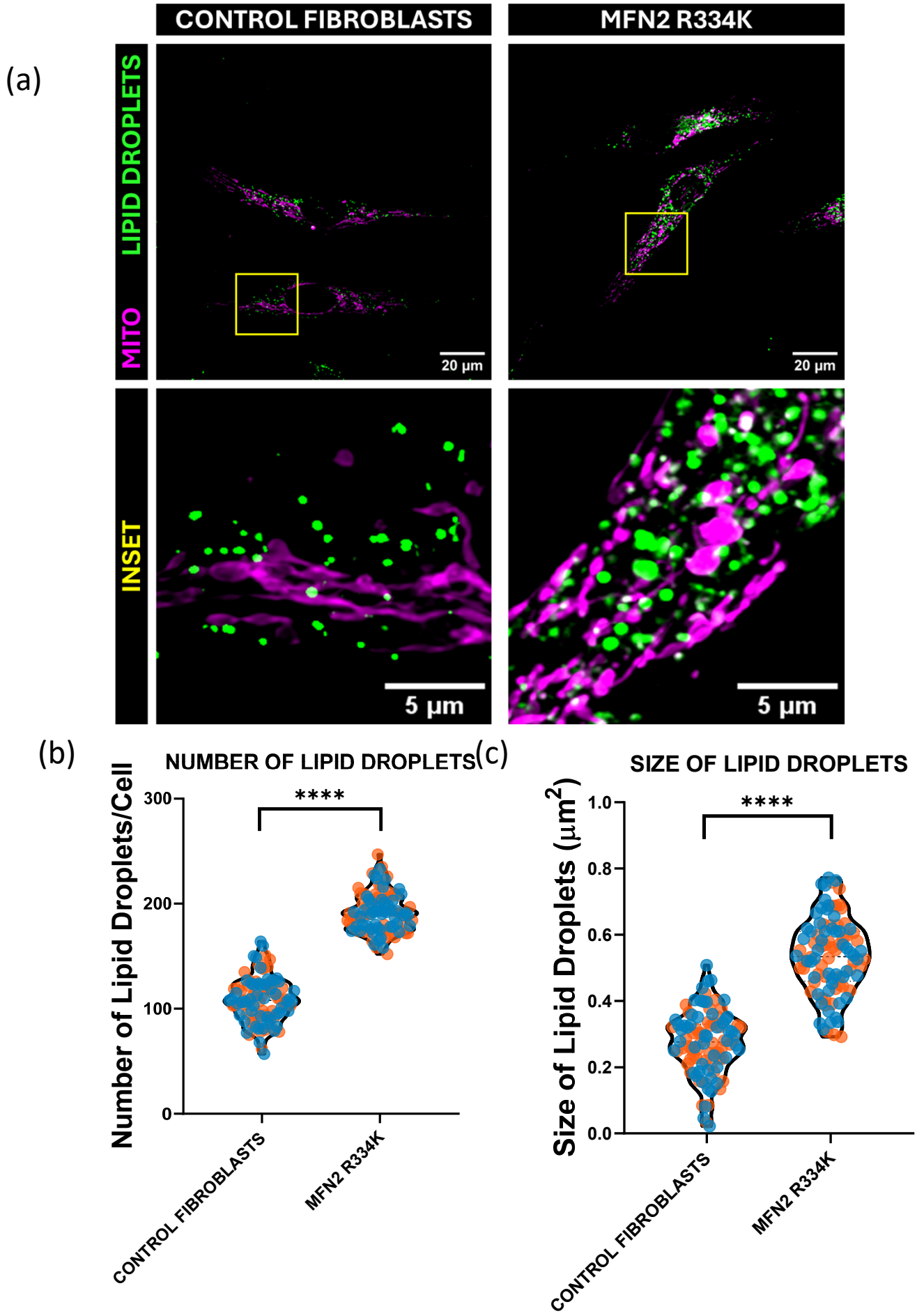
(a)
CONTROL FIBROBLASTS
MFN2 R334K
LIPID DROPLETS
MITO
INSET
20 µm
20 µm
5 µm
5 µm
(b)
NUMBER OF LIPID DROPLETS
Number of Lipid Droplets/Cell
300
200
100
0
****
CONTROL FIBROBLASTS
MFN2 R334K
(c)
SIZE OF LIPID DROPLETS
Size of Lipid Droplets (µm²)
1.0
0.8
0.6
0.4
0.2
0.0
****
CONTROL FIBROBLASTS
MFN2 R334K

Figure 5

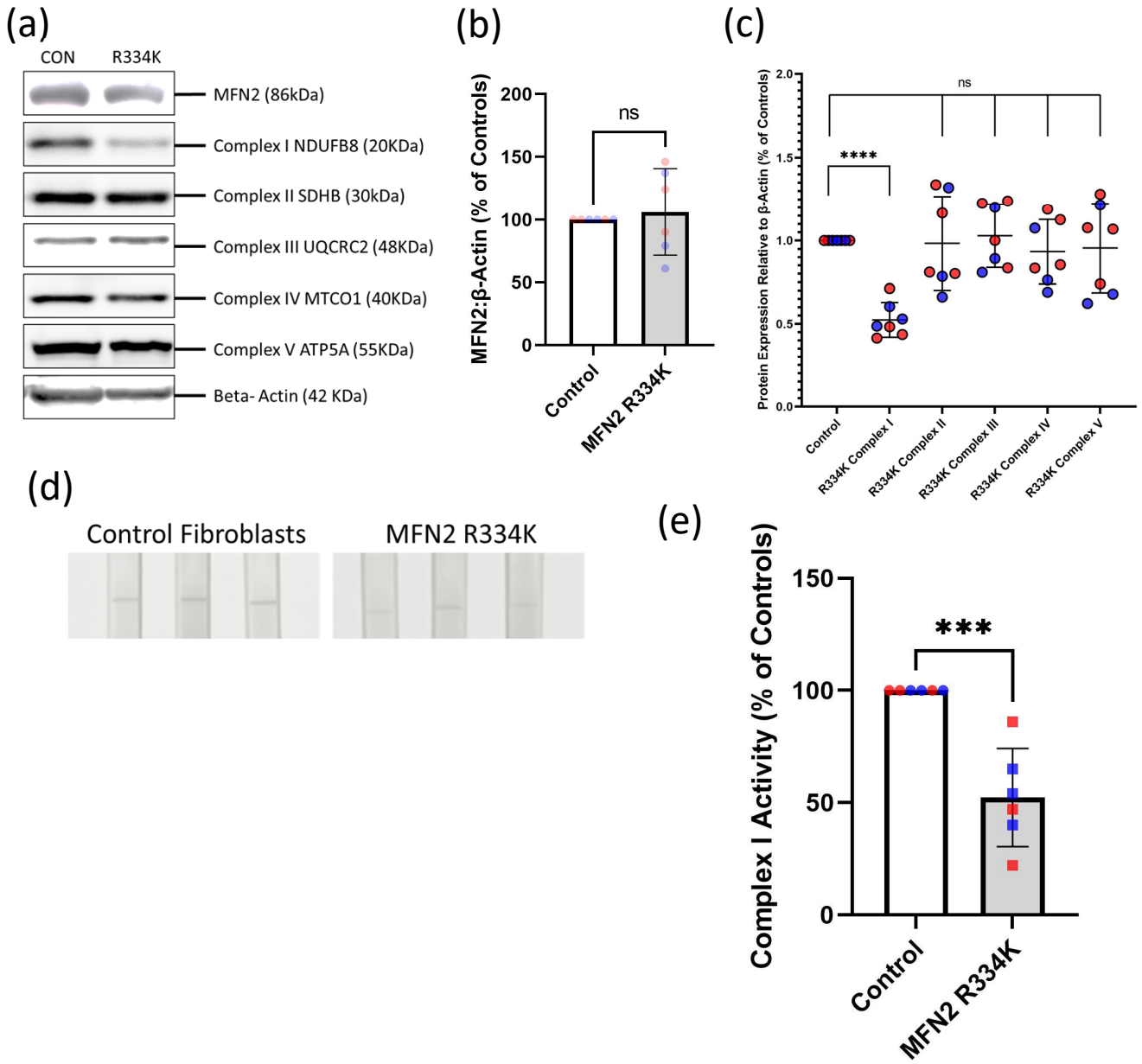
(a)
CON
R334K
MFN2 (86kDa)
Complex I NDUFB8 (20KDa)
Complex II SDHB (30kDa)
Complex III UQCRC2 (48KDa)
Complex IV MTCO1 (40KDa)
Complex V ATP5A (55KDa)
Beta- Actin (42 KDa)
(b)
MFN2:β-Actin (% of Controls)
200
150
100
50
0
ns
Control
MFN2 R334K
(c)
Protein Expression Relative to β-Actin (% of Controls)
2.0
1.5
1.0
0.5
0.0
ns
****
Control
R334K Complex I
R334K Complex II
R334K Complex III
R334K Complex IV
R334K Complex V
(d)
Control Fibroblasts
MFN2 R334K
(e)
Complex I Activity (% of Controls)
150
100
50
0
***
Control
MFN2 R334K

Figure 6

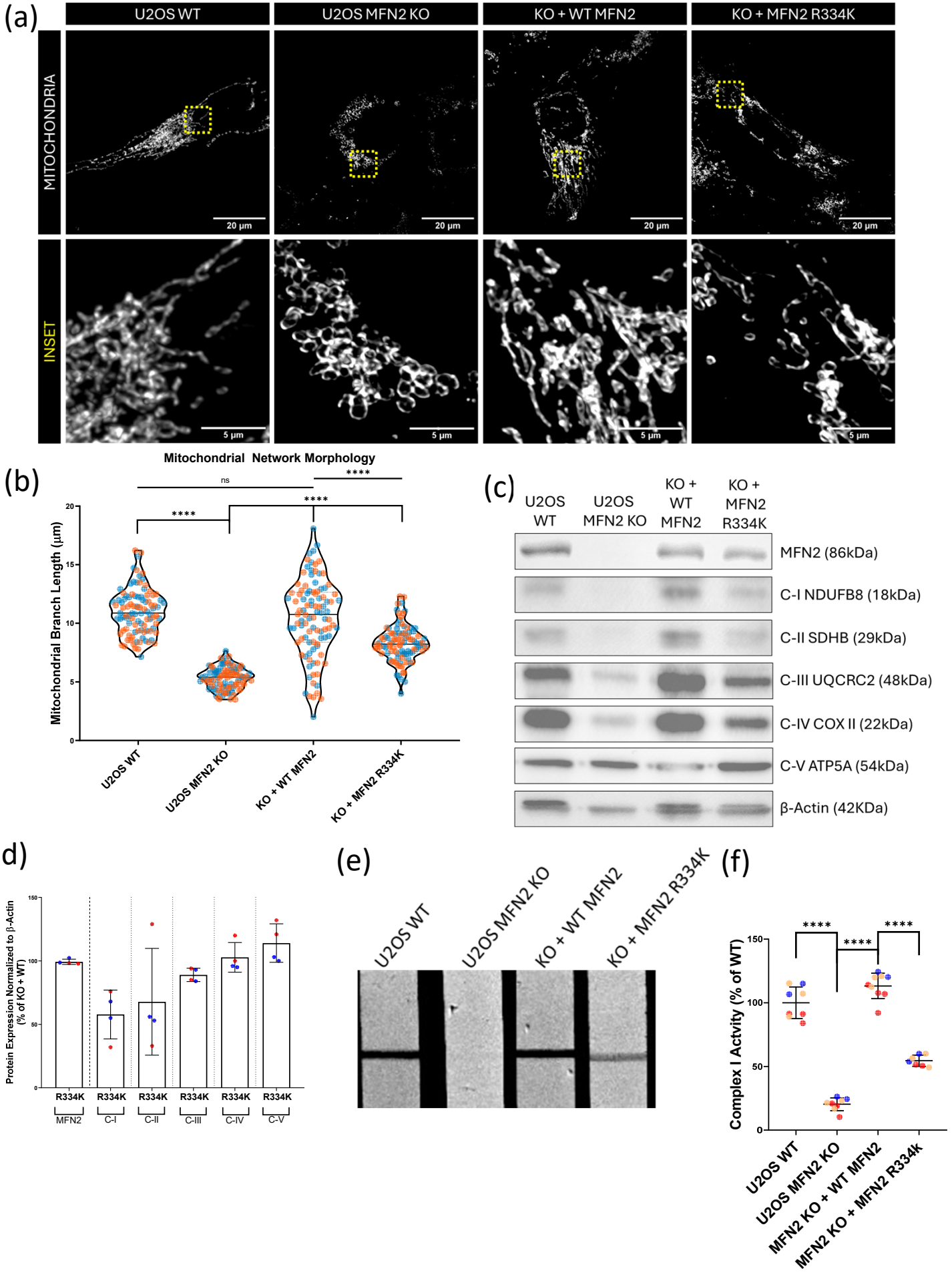
(a)
U2OS WT
U2OS MFN2 KO
KO + WT MFN2
KO + MFN2 R334K
MITOCHONDRIA
INSET
20 µm
5 µm
(b)
Mitochondrial Network Morphology
Mitochondrial Branch Length (µm)
ns
****
U2OS WT
U2OS MFN2 KO
KO + WT MFN2
KO + MFN2 R334K
(c)
U2OS WT
U2OS MFN2 KO
KO + WT MFN2
KO + MFN2 R334K
MFN2 (86kDa)
C-I NDUFB8 (18kDa)
C-II SDHB (29kDa)
C-III UQCRC2 (48kDa)
C-IV COX II (22kDa)
C-V ATP5A (54kDa)
β-Actin (42KDa)
(d)
Protein Expression Normalized to β-Actin (% of KO + WT)
R334K
MFN2
C-I
C-II
C-III
C-IV
C-V
(e)
U2OS WT
U2OS MFN2 KO
KO + WT MFN2
KO + MFN2 R334K
(f)
Complex I Activity (% of WT)
U2OS WT
U2OS MFN2 KO
MFN2 KO + WT MFN2
MFN2 KO + MFN2 R334k

Figure 7

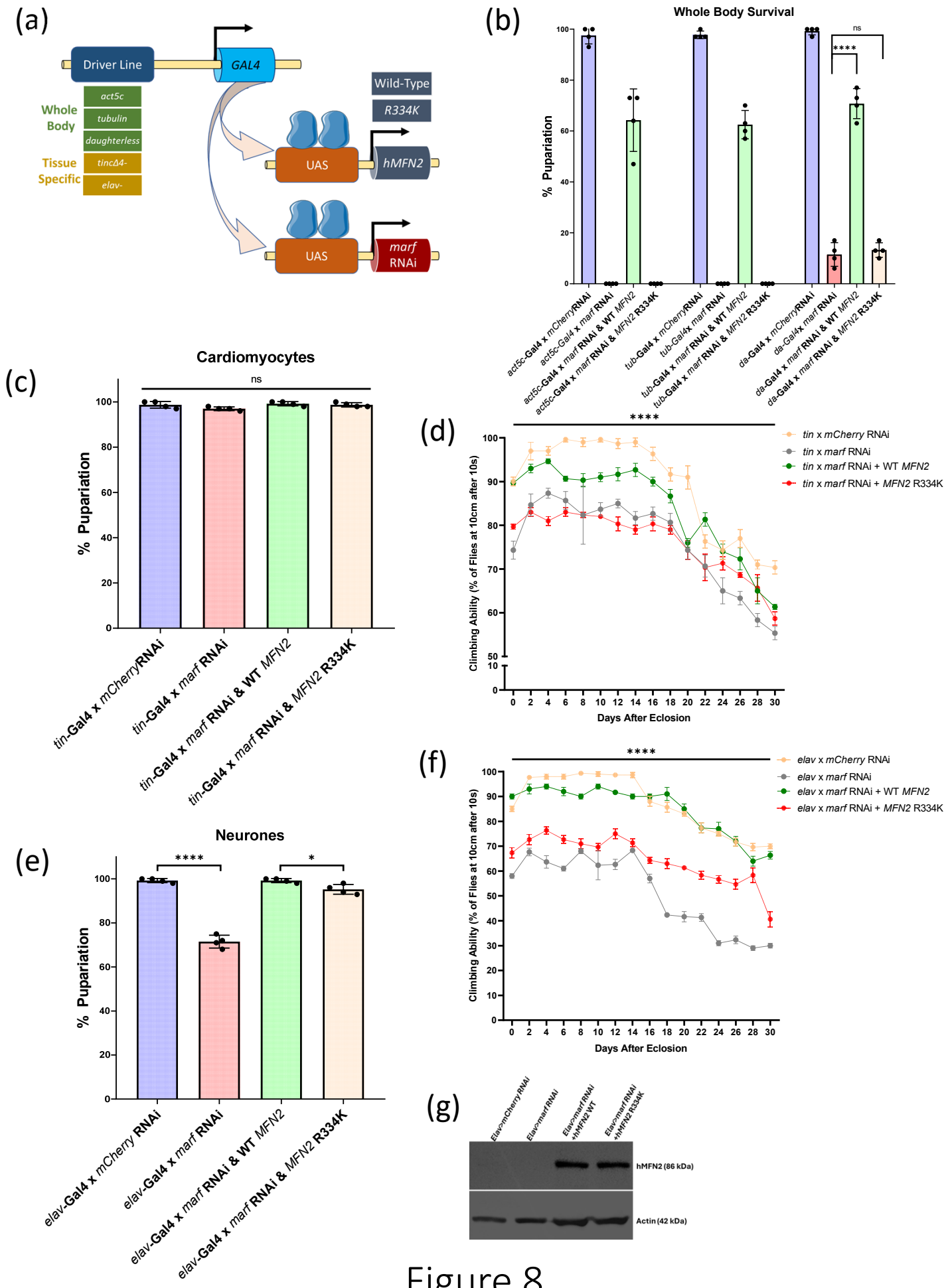
(a)
Driver Line
GAL4
Whole Body
act5c
tubulin
daughterless
Tissue Specific
tincΔ4-
elav-
Wild-Type
R334K
UAS
hMFN2
UAS
marf RNAi
(b)
Whole Body Survival
% Pupariation
ns
****
act5c-Gal4 x mCherryRNAi
act5c-Gal4 x marf RNAi
act5c-Gal4 x marf RNAi & WT MFN2
act5c-Gal4 x marf RNAi & MFN2 R334K
tub-Gal4 x mCherryRNAi
tub-Gal4x marf RNAi
tub-Gal4 x marf RNAi & WT MFN2
tub-Gal4 x marf RNAi & MFN2 R334K
da-Gal4 x mCherryRNAi
da-Gal4x marf RNAi
da-Gal4 x marf RNAi & WT MFN2
da-Gal4 x marf RNAi & MFN2 R334K
(c)
Cardiomyocytes
% Pupariation
ns
tin-Gal4 x mCherryRNAi
tin-Gal4 x marf RNAi
tin-Gal4 x marf RNAi & WT MFN2
tin-Gal4 x marf RNAi & MFN2 R334K
(d)
****
Climbing Ability (% of Flies at 10cm after 10s)
Days After Eclosion
tin x mCherry RNAi
tin x marf RNAi
tin x marf RNAi + WT MFN2
tin x marf RNAi + MFN2 R334K
(e)
Neurones
% Pupariation
****
*
elav-Gal4 x mCherry RNAi
elav-Gal4 x marf RNAi
elav-Gal4 x marf RNAi & WT MFN2
elav-Gal4 x marf RNAi & MFN2 R334K
(f)
****
Climbing Ability (% of Flies at 10cm after 10s)
Days After Eclosion
elav x mCherry RNAi
elav x marf RNAi
elav x marf RNAi + WT MFN2
elav x marf RNAi + MFN2 R334K
(g)
Elav>mCherryRNAi
Elav>marf RNAi
Elav>marf RNAi +hMFN2 WT
Elav>marf RNAi +hMFN2 R334K
hMFN2 (86 kDa)
Actin (42 kDa)

Figure 8

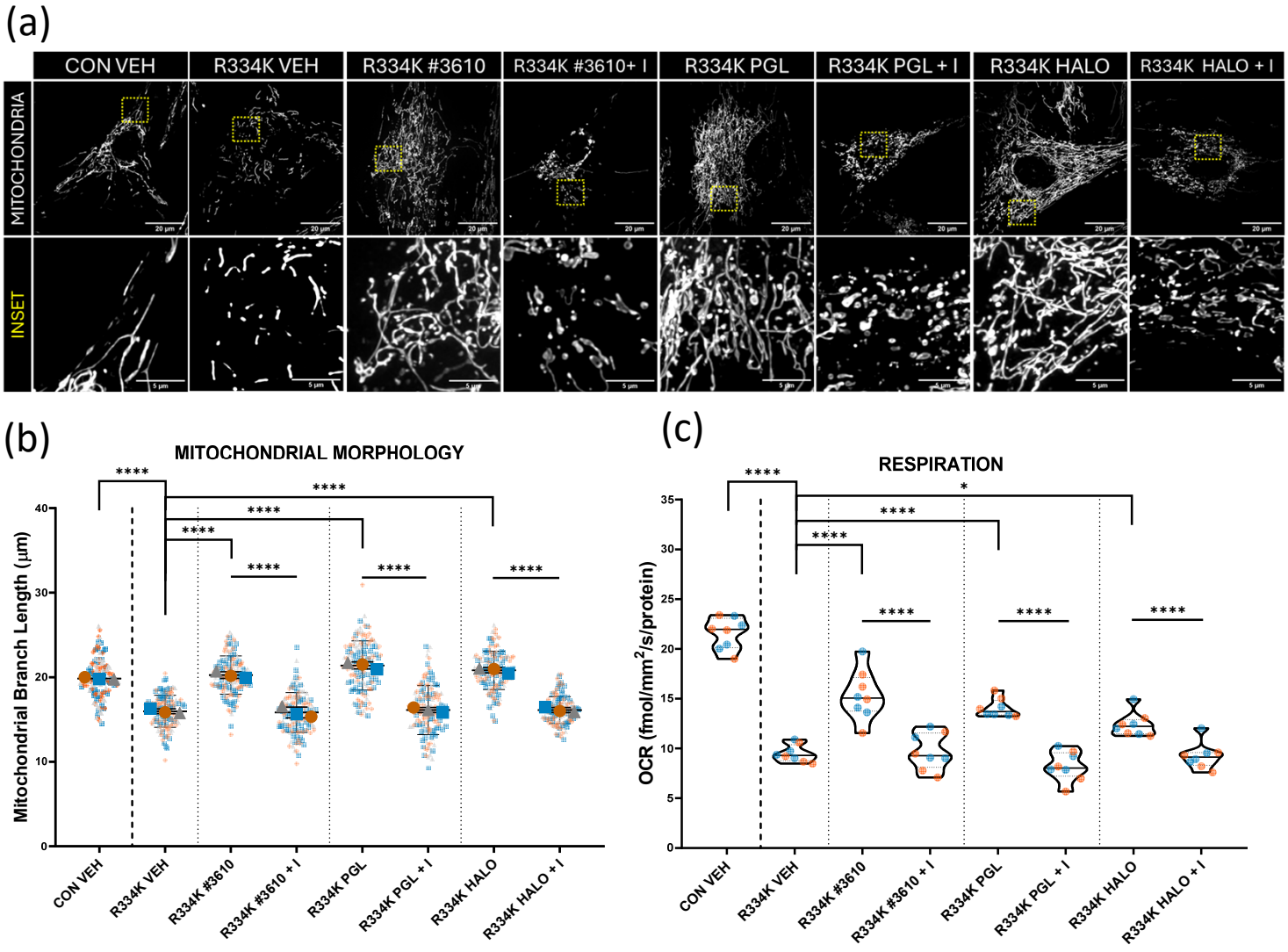
(a)
CON VEH
R334K VEH
R334K #3610
R334K #3610+ I
R334K PGL
R334K PGL + I
R334K HALO
R334K HALO + I
MITOCHONDRIA
INSET
(b)
MITOCHONDRIAL MORPHOLOGY
Mitochondrial Branch Length (µm)
(c)
RESPIRATION
OCR (fmol/mm²/s/protein)
CON VEH
R334K VEH
R334K #3610
R334K #3610 + I
R334K PGL
R334K PGL + I
R334K HALO
R334K HALO + I

Figure 9